LUND UNIVERSITY

Cross-modal Imaging in Lung Research: From µCT dosimetry to synchrotron phase contrast microtomography biomechanical insights in preclinical lung injury models

Deyhle Jr, Richard

2024

Document Version:
Publisher's PDF, also known as Version of record

Cross-modal Imaging in Lung Research

From µCT dosimetry to synchrotron phase-contrast in-vivo microtomography biomechanical insights in pre-clinical lung injury models

RICHARD THOMAS DEYHLE JR.
DEPARTMENT MEDICAL RADIATION PHYSICS, MALMÖ | LUND UNIVERSITY

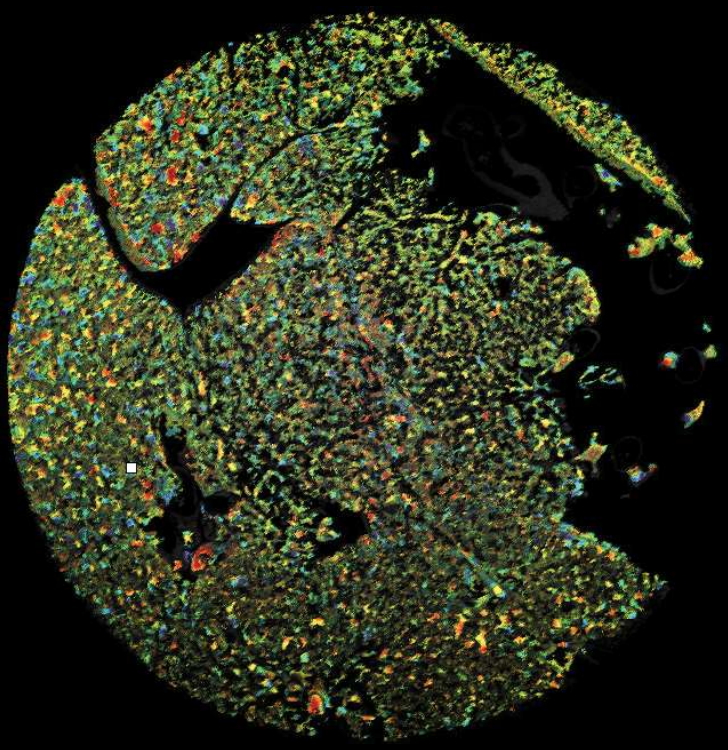

Cross-modal Imaging in Lung Research

From μCT dosimetry to synchrotron phase-contrast *in-vivo* microtomography biomechanical insights in pre-clinical lung injury models

Richard Thomas Deyhle Jr.

LUND
UNIVERSITY

LICENTIATE DISSERTATION

Licentiate dissertation for the degree of Licentiate (Lic.) at the Faculty of Medical Radiation Physics, Malmö at Lund University to be publicly defended on date of 19th of April at 14:15 in Room 2005, Department of Medical Radiation Physic, Malmö, Skåne University Hospital Carl-Bertil Laurells gata 9, Elevator Hall C, Floor 2

Faculty opponent

Dr. Leif Hultin PhD, In Vivo Imaging Sciences, BioPharmaceuticals R&D, Clinical Pharmacology & Safety Sciences, AstraZeneca, Mölndal, Sweden

Organization LUND UNIVERSITY	**Document name** **LICENTIATE DISSERATION**
	Date of issue **March 28 2024**
Author(s) Richard Thomas Deyhle Jr.	Sponsoring organization

Title and subtitle

Cross-modal Imaging in Lung Research: From µCT dosimetry to synchrotron phase-contrast *in-vivo* microtomography biomechanical insights in pre-clinical lung injury models

Abstract

Lung diseases continue to present a large burden to public health, especially in industrialized countries. For a better understanding of the underlying patho-mechanisms in lung related diseases as well as for testing the efficacy of novel therapies, preclinical studies in animal models are indispensable. The significance of preclinical X-ray based micro-computed tomography (µCT) research lies in its ability to provide high-resolution, non-invasive lung imaging of small animals as the air inside the lung acts as a natural contrast and to image the lung parenchyma longitudinally to assess functional and morphological alterations and test efficacy of therapeutic interventions. This often requires requires imaging protocols that balance between sufficient image quality and clinically relevant radiation absorbed doses. A reproducible method for evaluation of absorbed radiation absorbed doses is desirable. Absorbed radiation absorbed doses were measured in a polymethyl methacrylate (PMMA) phantom using standard TLD and a novel type of OSLD made form household salt. Four imaging protocols from MILabs “xUHR-µCT” scanner were tested. A large discrepancy was observed from results compared to vendor-provided values. The results indicate a need for thorough empirical dose measurements prior to performing longitudinal studies.

Four-dimensional imaging, allows for investigation of the dynamics of regional lung functional parameters simultaneously with structural deformation of the lung as a function of time. It is of significant interest to have direct visualization and quantification of interstitial lung diseases at spatial resolutions beyond the capabilities of clinical and conventional absorption-based only CT. Thus far, the high intensity of synchrotron X-ray light sources offer a tool to investigate dynamic morphological and mechanistic features, enabling dynamic *in-vivo* microscopy. This investigation elucidates the direct effects of interventions targeting the pathophysiology of Acute Respiratory Distress Syndrome (ARDS) and Ventilator-Induced Lung Injury (VILI) on the terminal airways and alveolar microstructure within intact lungs. In such conditions, the relationship between microscopic strain within the mechanics of the alveolar structure and the broader mechanical characteristics and viscoelastic properties of the lungs remains poorly understood. A time-resolved synchrotron phase-contrast micro-computed tomography imaging acquisition protocol based on the synchronization between the mechanical ventilation and the cardiac activity was used to resolve the lung parenchyma motion with an effective isotropic voxel size of 6 µm. Quantitative maps of microscopic local lung tissue strain within aereated lung alveolar tissue under protective mechanical ventilation in anesthetized rats were obtained. This approach was used to assess the effect of alterations in lung tissue biomechanics induced by lung injury at 7 days after single-dose, intratracheal bleomycin instillation in combination with short-term high-tidal volume (VT) mechanical ventilation. Overall, this work address the aspects of radiation exposure to in experimental imaging of small animals and lays a foundation for a more nuanced understanding of lung injury and mechanical ventilation. In the future, it may result in a more effective and less injurious respiratory support for patients with acute lung injury or chronic lung diseases.

Key words TL, OSL, computed tomography, phantoms, X-rays, pre-clinical, dosimetry: physical basis, biomedical strain, lung injury, mechanical ventilation, inflammation, lung function, synchrotron, FOT, histology

Classification system and/or index terms (if any)

Supplementary bibliographical information		**Language** English
ISSN and key title 1652-8220		**ISBN** 978-91-8021-558-9
Recipient’s notes	**Number of pages** 68	Price
	Security classification	

Signature Richard T. Deyhle Jr. Date 2024-04-19

Cross-modal Imaging in Lung Research

From μCT dosimetry to synchrotron phase-contrast *in-vivo* microtomography biomechanical insights in pre-clinical lung injury models

Richard Thomas Deyhle Jr.

LUND
UNIVERSITY

Faculty of Medicine
Department Medical Radiation Physics, Malmö

ISBN 978-91-8021-558-9

Printed in Sweden by Media-Tryck, Lund University
Lund 2024

To my family for their unwavering support

Table of Contents

Abstract

Lung diseases constitute a major burden on society and patients. To quantify the underlying patho-mechanisms in lung diseases as well, to test the efficacy of novel therapies, preclinical studies in *in-vivo* animal models are indispensable. The significance of preclinical X-ray based micro-computed tomography research is the ability to provide high-resolution, non-invasive, quantifiable longitudinal assessment of lung parenchyma, functional changes and therapeutic efficacy. This often requires requires imaging protocols that balance between sufficient image quality and clinically relevant radiation absorbed doses. A reproducible method for evaluation of absorbed radiation absorbed doses is desirable. Absorbed radiation absorbed doses were measured in a PMMA phantom using standard TLD and a novel type of OSLD made from household salt. Four imaging protocols from MILabs "xUHR-µCT" scanner were tested. A large discrepancy was observed from results compared to vendor-provided values. The results indicate a need for thorough empirical dose measurements prior to performing longitudinal studies. Four-dimensional imaging, allows for investigation of the dynamics of regional lung functional parameters simultaneously with structural deformation of the lung as a function of time. It is of significant interest to have direct visualization and quantification of interstitial lung diseases at spatial resolutions beyond the capabilities of clinical and conventional absorption-based only CT. Thus far, the high intensity of synchrotron X-ray light sources offer a tool to investigate dynamic morphological and mechanistic features, enabling dynamic *in-vivo* microscopy. This investigation elucidates the direct effects of interventions targeting the pathophysiology of Acute Respiratory Distress Syndrome and Ventilator-Induced Lung Injury on the terminal airways and alveolar microstructure within intact lungs. In such conditions, the relationship between microscopic strain within the mechanics of the alveolar structure and the broader mechanical characteristics and viscoelastic properties of the lungs remains poorly understood. A time-resolved synchrotron phase-contrast micro-computed tomography imaging acquisition protocol based on the synchronization between the mechanical ventilation and the cardiac activity was used to resolve the lung parenchyma motion with an effective isotropic voxel size of 6 µm. Quantitative maps of microscopic local lung tissue strain within aereated lung alveolar tissue under protective mechanical ventilation in anesthetized rats were obtained. This approach was used to assess the effect of alterations in lung tissue biomechanics induced by lung injury at 7 days after single-dose, intratracheal bleomycin instillation in combination with short-term high-tidal volume mechanical ventilation. Overall, this work addresses the aspects of radiation exposure to in experimental imaging of small animals and lays a foundation for a more nuanced understanding of lung injury and mechanical ventilation. In the future, it may result in a more effective and less injurious respiratory support for patients with acute lung injury or chronic lung diseases.

Popular scientific summary in Swedish

I preklinisk forskning, dvs. den forskning som utförs före den kliniska forskningen, används ofta smådjur; vanligtvis råttor och möss. När man utför denna typ av försök, så är det viktigt att få ut så mycket information som möjligt samtidigt som man ser till att djuren mår bra och även att man använder så få försökdjur som möjligt. För att uppnå detta är det mycket viktigt att optimera sina försök genom att använda så skonsamma metoder som möjligt för djuren samtidigt som försöken ger resultat på flera nivåer, exempelvis på både mikro- och makronivå. När det gäller preklinisk forskning på smådjur, så är olika typer av bildtagningsmetoder mycket värdefulla eftersom det ger en ögonblicksbild av ett eventuellt sjukdomsförlopp och möjlighet att följa sjukdomens progress i samma djur över tid med bildtagning vid olika tidpunkter i förloppet.

Två röntgen-baserade bildtagningsmetoder, som ger resultat på olika spatial nivå, är bildtagning med μCT (micro Computed Tomography) och synkrotron-baserad bildtagning. Dessa tekniker kompletterar varandra och ger olika typer av information. Exempelvis så är μCT:n optimal för användning i longitudinella studier där man, som tidigare nämnts, tar bilder av samma djur vid olika tidpunkter. Fördelen med denna typ av studieupplägg är att resultaten i en mätserie inte påverkas av individuella skillnader mellan försöksdjuren. Man har också möjlighet att ta bilder av hela eller delar av kroppen, och kan då få en uppfattning om hur sjukdomen påverkar hela organ eller organsystem, som exempelvis här; i lungorna. Ett problem som man dock måste ta hänsyn till när det gäller t ex. lungsjukdomar, är stråldosen som djuret får vid varje bildtagning. Stråldosen kan, om den blir väldigt hög, påverka sjukdomsförloppet och på så vis påverka resultaten av en longitudinell studie. Därför är det mycket viktigt att som ett led i planeringen av en sådan studie, uppskatta vilka ståldoser djuren får vid varje mätning, och minimera dessa så långt det är möjligt med bibehållen bildkvalitet.

Många läkemedel kan ge lungskador som en bieffekt av behandlingen och långvarig användning av ventilator kan ge skador på lungorna. Med synkrotron-baserad bildtagning kan man uppnå en väsentligt högre bildupplösning och kontrast än med μCT, för mycket små volymer. Detta gör att dessa tekniker kompletterar varandra, och sjukdomsförloppet som kan ses i ett större sammanhang med hjälp av μCT (t ex. fibros i lungan), kan studeras i detalj på vävnadsnivå vid synkrotron-baserad bildtagning, för att se förändringar i elasticitetsparametrar i lungvävnad vid olika typer av inducerad lungskada.

Original Articles

This work is based on the following papers, which will be referred to in the text by their Roman numerals:

I. "Development of a robust and reproducible method for evaluation of absorbed doses in preclinical *in-vivo* μCT studies" R.T. Deyhle Jr, C. Bernhardsson, L.E. Olsson, M. Sydoff, Manuscript submitted to Radiation Protection and Dosimetry

II. "*In-Vivo* Synchrotron Phase-Contrast Imaging of Lung Tissue Biomechanics In a Rat Model of Ventilator and Bleomycin-Induced Injury" R.T. Deyhle Jr., L. Fardin, I.M. Persson, J.L. Cercos-Pita, G. Perchiazzi, L.E. Olsson, S. Bayat, Manuscript

Preliminary reports

Preliminary reports have been presented at the following international meetings and conferences:

- **DOSIMETRY CONCEPTS FOR QUALITY ASSURANCE IN μCT (poster presentation)**
  Richard Deyhle Jr., Christian Bernhardsson, Lovisa Waldner, Lars E. Olsson, Marie Sydoff
  International conference of Medical Physics in the Baltic States 15, Kaunas, Lithuania, 2021

- **DOSE VERIFICATION AND IMPROVED METHOD DEVELOPMENT FOR DOSE OPTIMIZATION FOR *IN-VIVO* μCT (oral presentation)**
  Richard Deyhle Jr., Christian Bernhardsson, Lovisa Waldner, Lars E. Olsson, Marie Sydoff
  International conference of Nordic Society for Radiation Protection (NSFS), Malmö, Sweden, 2023

- **Investigating local tissue deformation using *in-vivo* 4D synchrotron X-ray μ-CT in bleomycin-induced lung injury in rats (poster presentation)**
  Richard Deyhle Jr., Luca Fardin, Irma Mahmutovic Persson, Jose L. Cercós, Anders Larsson, Gaetano Perchiazzi, Lars E. Olsson, Sam Bayat
  International conference of European Society of Biomechanics, Maastricht, The Netherlands, 2023

- **Investigating local tissue deformation using *in-vivo* 4D synchrotron X-ray µ-CT in ventilator-induced lung injury in combination with bleomycin-induced lung injury in rats (oral presentation)**
  Richard Deyhle Jr., Luca Fardin, Irma Mahmutovic Persson, Jose L. Cercós, Geatano Perchiazzi, Lars E. Olsson, Sam Bayat
  International conference of European Society of Molecular Imaging, Porto, Portugal, 2024

List of abbreviations and symbols

ARDS – Acute Respiratory Distress Syndrome

CMOS - Complementary metal-oxide-semiconductor

CNR – Contrast to noise ratio

CT – Computed Tomography

μCT – Micro-Computed Tomography

DILD – Drug-induced interstitial lung disease

ϵ – Biomechanical strain

$\dot{\varepsilon}$ – Biomechanical strain rate

ECG – Electrocardiogram

ECM – Extracellular Matrix

ESRF – European Synchrotron Radiation Facility

L-FOT – Low-frequency Forced Oscillation Technique

FPS – frame rates per second

G – Damping

H - Elastance/dissipation

HRCT – High Resolution Computed Tomography

I.T. – Intratracheal instillation

ITK – Insight Toolkit

LFOT – Low-frequency Forced Oscillation Technique

MCP-N – Ultra sensitive thermoluminscent LiF

MLS – Mean least squared

MOSFET – Meta-oxide-semiconductor field-effect transistor

MTF – Modular Transfer Function

MV – Mechanical Ventilation

η – Hysterisitivity

OSLD – Optically stimulated luminescence dosemeter

PCO – Pioneering in Cameras and Optoelectronics

PEEP – Positive end-expiratory pressure

PF – Pulmonary Fibrosis

PIRT – Python Image Registration Toolkit

PMT – Photomultiplier Tube

RR – Respiratory Rate

SDD – Source to detector distance

SID – Source to Image distance

SNR – Signal to noise ratio

Sr-μCT – Synchrotron micro-Computed Tomography

TLD – thermoluminescence detector

TSL – thermally stimulated luminescence

VILI – Ventilator Induced Lung Injury

VT – Volume tidal

VTK – Visualization Toolkit

Z_{eff} – Effective Proton number

4DCT – four-dimensional computed tomography

Introduction

Small animal *in-vivo* imaging plays an essential role in preclinical research aimed at understanding clinically relevant research questions regarding physiological processes, disease progression and therapeutic management. Microscopic X-ray based Computed Tomography (μCT) is one of the most commonly used imaging technologies in preclinical research. It provides detailed anatomical information about the volume, textures and abnormal alterations of internal structures in high spatial resolution, providing dynamic information of the lung dynamics when time-resolved data is acquired. Micro-computed tomography (μCT) from both laboratory and synchrotron sources has proven to be an invaluable asset to non-invasively obtain morphological and functional three-dimensional information of the lungs.

Many aspects are common to both pre-clinical μCT and synchrotron μCT (Sr-μCT) systems. μCT and Sr-μCT systems both provide useful information of the morphology, volume and function of the lung structure. When the same animal models have been applied to both imaging modalities, the reason for one over the other depends rather on the intended research question and the spatial and temporal scale required to visualize the desired physical phenomenon. One major distinction is commercial preclinical μCT scanners are often designed for fast low-dose scans and high-throughput studies. Whereas synchrotron applications of μCT are designed for maximum spatial resolution and contrast, offering long propagation distances required for phase-contrast imaging.

Imaging the microstructure and micromechanics of the tissues of animals *in-vivo* is a challenging task. The high spatial resolution required in these studies may result in a high absorbed dose to the animals. Using μCT imaging for longitudinal studies could be problematic due to the radiation burden that repeated imaging may induce. The absorbed doses could in some cases be on the order of magnitude as to bias experimental results but also impacts their clinical relevance, thereby influencing the interpretation of these outcomes. To optimize μCT acquisition parameters, it is essential to keep the absorbed dose low without sacrificing image quality.

To address this, pre-clinical dosimetry studies are available in the literature (Meganck and Liu, 2017; Mannheim *et al.*, 2019) with pre-clinical μCT doses reported through Monte Carlo calculations (Deak and Kalender, 2009; Li, Zhang and Liu, 2013) or experimental measurements with thermo-luminescent dosemeters (TLD) (Figueroa *et al.*, 2008) and optically stimulated luminescent dosemeters

(OSLD) (Willekens *et al.*, 2010). Both post-mortem animal studies and those using phantoms to mimic specific animals have been conducted. Measurements in phantoms have the advantage of being easily repeated in a well-defined geometry. Though, the results of these studies are not generalizable. The results of Study **I** are an attempt to address these limitations.

Investigating radiation absorbed doses for *in-vivo* x-ray μCT imaging studies is vital for several reasons. Firstly, it is important to understand and quantify the actual radiation absorbed dose delivered during imaging to minimize the risk of harmful effects. Secondly, in longitudinal studies, cumulative radiation absorbed doses can become significant and may affect animal health which could affect study results. Thirdly, the validity and reliability of the collected data in small animal imaging directly determine the benefits derived from such studies. Accurate knowledge of the radiation absorbed dose is crucial for optimizing imaging protocols and image quality.

One critically important application of preclinical μCT is to facilitate research studies that probe clinically relevant questions unfeasible in human subjects. This is particularly vital when investigating the intricacies of lung anatomy and function at resolutions capable of visualizing the alveolar scale, which necessitates radiation absorbed doses far beyond the safe limits for human exposure. The dual objectives of μCT in this context embrace distinct yet complementary philosophies:

1. Minimization of radiation absorbed dose without compromising the image quality necessary to accurately address clinically relevant questions.
2. The imperative to maximize spatial resolution and contrast with temporal resolutions that allow the capability to investigate the dynamic mechanics of the lung at the micrometer scale.

In this work, Study **II**, addresses the gap that persists in linking global lung mechanics to the microscopic tissue strain in the lung acinus during the dynamic process of lung inflation in injured lungs. This is a complex relationship that remains poorly understood in both pathological conditions and in the normal, healthy lung. As highlighted by Nieman (2012), traditional methodologies have primarily relied on observations of lungs fixed at a single inflation state. These static approaches significantly limit our ability to comprehend the dynamic interactions and the mechanical behavior of the lung at different levels of inflation. To overcome this, assessment of global mechanical load was performed using the low-frequency Forced Oscillation Technique (L-FOT). This method allows for the characterization of respiratory compliance, impedance, resistance and resonant frequency, providing valuable insights into lung function with minimal cooperation required from the patient.

The technical limitations of direct observation of the dynamics of the lung parenchyma at the level of the terminal airways and alveoli during mechanical

ventilation where spatial scales are less than 10 μm have only been achieved by synchrotron radiation phase-contrast 3D microscopy (Lovric *et al.*, 2018; Cercos-Pita *et al.*, 2022).

To achieve 4D *in-vivo* imaging with high spatial resolution and temporal resolution the radiation absorbed dose will be too high using a μCT. For such studies synchrotron micro-imaging offers an attractive alternative. The radiation absorbed dose is lower to the animal using synchrotron imaging compared to pre-clinical μCT X-ray imaging due to the unique properties of synchrotron radiation. Synchrotron radiation is highly brilliant and energy-selective, allowing for more efficient imaging with lower doses of radiation. This efficiency stems from the ability to use monochromatic X-ray beams, which can be precisely tuned to the optimal energy for minimizing dose while maximizing image contrast and resolution. As a result, synchrotrons, which are circular particle accelerators that speed up charged particles with magnets to produce intensely bright light primarily in the X-ray spectrum, are considered the "gold standard" in visualizing dynamic processes at the alveolar scale. They provide a quasi-monochromatic, tuneable light source that is millions of times brighter than traditional X-ray sources, facilitating high-spatial resolution imaging without the need for high doses of radiation.

In this work, Study **II** predicated on prior advancements in image acquisition, development of a custom retrospective gating strategy and image analysis. Initially, a 4D dynamic phase-contrast computed micro-tomography (4D-μCT) technique using synchrotron radiation initially developed by Mokso et. Al. (Mokso *et al.*, 2015), was adapted to gate the cardiac cycle, while being triggered by the forced respiratory motion controlled from a mechanical ventilator. For the first time, allowing for dynamic *in-vivo* microscopy in the lungs of small animals with sufficient spatial resolution and contrast to investigate in deep lung acini and individual alveoli with temporal resolutions able to capture *in-vivo* dynamic conditions (Smaldone and Mitzner, 2012). Achieving an isotropic voxel size of 6 μm (Cercos-Pita *et al.*, 2022), We applied this technique to investigate an animal model of Acute Respiratory Distress Syndrome (ARDS) by intratracheally injection of bleomycin. In combination with Ventilator-Induced Lung Injury (VILI) induced by short-term high tidal-volume injurious mechanical ventilation. We applied this methodology to acquire maps of strain distribution due to positive-pressure breaths in the lung acini.

The overall mortality in ARDS patients is between 35- 45% (Bellani *et al.*, 2016b), instigating many unanswered questions. In models of ARDS, progression of injury increases the local strain on the lung tissue through several mechanisms such as hyperinflation, atalectrauma, and associated inflammation and fibrosis . However, the magnitude and distribution of strain imposed on the peripheral airspaces by mechanical ventilation at the microscopic level and the resulting deformation of alveoli and acini are poorly understood, despite their importance for unraveling the mechanisms occurring at the onset of VILI. Specifically, how microscopic strain is

related to the overall respiratory mechanical parameters and viscoelastic behaviour in the injured lung is not well understood.

Aims

The overall objective of this work was to use advanced imaging techniques such as conventional μCT and synchrotron phase-contrast imaging and tackling the challenges that could arise when studying lung disease at different levels.

In Study **I**, the main purpose was to initially benchmark results from the TLDs and NaCl pellets and to compare these results with the vendor-provided dose values for the four default imaging protocols. A secondary purpose was to demonstrate that this method can easily be adaptable to other laboratories and equipment. Given the lack of standardization in preclinical data acquisition, it is of great importance to develop approaches that accelerate the acquisition of accurate, reproducible, highly sensitive and dynamic preclinical data intended for *in-vivo* rodents. It is important to address these challenges by developing and adopting standardized methodologies in this area.

In Study **II**, the main purpose was to investigate how early stages of bleomycin induced lung injury in combination with short-term high-tidal volume (VT) affect local microscopic strain distribution in the lung airspaces. To assess this, we obtained dynamic quantitative maps at an isotropic voxel resolution of 6 μm in anesthetized rats before and after they had undergone lung injury. The relation between microscopic strain and overall respiratory mechanical parameters and viscoelastic behaviour in injured lungs was investigated. Providing a comprehensive investigation to elucidate the direct impact on the biomechanical dynamics of lung injury. The rationale behind this study was to improve the understanding of how lung injury and mechanical ventilation affect the local microscopic strain within the lung to provide insights into the microscopic changes that occur in lung tissue, which could lead to improved mechanical ventilation strategies and treatments for lung injury.

Background

Lung imaging

The complex structure of the lung is continuously displaced by two main sources of motion: (i) breathing (spontaneous or through mechanical ventilation), and (ii) cardiovascular pulsation. To achieve micrometric spatial precision in dynamic 3D microscopy, two critical criteria must be met to ensure that the reconstructed tomography is devoid of motion artefacts. Firstly, the sample's local movement during the time it takes to capture a single projection must be less than the size of one pixel. This means that to accommodate increased spatial resolution and keep motion blur to a minimum, the time allotted for each projection's capture must be reduced in correlation with the motion's speed. To compensate for the shorter acquisition times while preserving the quality of each pixel—which directly influences the image's signal-to-noise ratio and thus the clarity of details—a significantly high X-ray flux is essential. Such flux levels are typically only achievable with synchrotron facilities. Secondly, ensuring that the sample and the acquisition system are in sync is imperative. Ideally, the sample would exhibit a perfectly periodic motion, allowing for the capture of a parallel projection at the same phase in each cycle.

Clinically, pulmonary fibrosis (either acute or idiopathic) is commonly diagnosed using physiological measurements such as pulmonary function tests in combination with visual radiological assessment high-resolution CT (Best *et al.*, 2008). Histological changes in the alveoli and airways, which are visually seen as honeycombing, increased fibrotic deposition and inflammation can be identified using high-resolution computed tomography (HRCT). This is performed by radiologists who measure the area of the lung occupied by regions of honeycombing, consolidation, hazy opaque regions (termed ground glass opacity), and abnormal reticular changes (Cozzi *et al.*, 2021). This established visual scoring method is commonly used in disease staging to predict mortality. The use of quantitative image-derived metrics from CT analysis is of significant interest in diagnosing and predicting outcomes in fibrotic lung diseases (Humphries *et al.*, 2022; Kunihiro *et al.*, 2023). In pre-clinical animal models, pulmonary fibrosis is often drug-induced using the chemotherapy agent Bleomycin (Liu, De Los Santos and Phan, 2017).

The fundamental operating concept of CT, which involves reconstructing the specimen's cross-sectional images from angular distributed projection images, necessitates the object to remain motionless during the data acquisition process. Motion induced by the heart and breathing, if left uncompensated, will results in motion artefacts, causing blurring. A method known as "gating" offers the opportunity to synchronize image capture with physiological motion, such as respiratory and cardiac motion with the tomographic acquisition. Different strategies of gating can be used: (i) imaging in breath-hold (Namati *et al.*, 2006), (ii) prospective gating (Ford *et al.*, 2005), and (iii) retrospective gating (Low *et al.*, 2003; Vedam *et al.*, 2002; Ford *et al.*, 2003). Breath-hold imaging in animal studies requires necessitates intubation and artificial ventilation. A physiological signal describing the phase of the motion is required to for gating. For the heart, the timing relies on the electrocardiogram signal (ECG), specifically the R wave, which marks the ventricular depolarization preceding the heart's contraction. The interval from one R wave to the next is used to determine the cardiac cycle's phase. Similarly, for capturing the lung's movements due to respiration, the process requires tracking the respiratory cycle. This is achieved by using sensors or markers to track the cheat wall movement or airflow, providing a signal that correlates with the phases of inhalation and exhalation. Synchronizing both ECG and respiratory gating for lung movement allows for highly detailed and motion-artefact-free imaging which is crucial to capture dynamic micrometric motion. The approaches found in the literature can be divided into two classes: prospective and retrospective gating.

In the method known as **prospective gating**, a physiological signal (e.g. ECG, respiratory rate), is monitored and evaluated concurrently with the process of tomographic imaging. This method triggers the capture of a projection precisely when a specific phase of interest occurs. The primary benefits of this technique include: (i) the sample is exposed to radiation exclusively during the targeted phase, which minimizes the risk of radiation-induced damage; and (ii) the imaging acquisition is timed in synch with the physiological motion, ensuring that the time resolution is solely dependent on the duration it takes to acquire each projection. The time resolution is here defined as the time interval associated to a single phase during the reconstruction.

In **retrospective gating**, the physiological signal is continuously recorded throughout the tomographic imaging process, and analysed after acquisition (a-posteriori). During the process, the projections are captured at a constant frame rate, without synchronizing with the physiological motion, such as breathing or heartbeats. In the reconstruction phase of tomography, the recorded physiological signal is then reviewed to determine the motion phase corresponding to each projection. The key difference with respect to prospective gating is that retrospective gating allows for capturing multiple phases of the motion within a single scan. This results in a 4-dimensional dataset (3D + time) at the cost of a reduced time resolution. The time resolution is limited by the acquisition time and reciprocal of

the frame rate of a projection. The downside of retrospective gating is the necessary sufficiently higher number of projections acquired which results in a higher radiation burden. However there are immediate effects of the radiation that have been reported including acute inflammation of the alveoli and pulmonary fibrosis within several weeks (Giuranno *et al.*, 2019).

These motion-compensation gating techniques have been applied for regional lung function investigations with both clinical CT scanners (Drangova *et al.*, 2007), μCT scanners (Preissner *et al.*, 2018; Jacob *et al.*, 2013) and synchrotron facilities (Dubsky *et al.*, 2012). Breath-hold and prospective gating techniques do not allow to capture the complete dynamic viscoelastic properties of the lung cycle. Accepting these limitations, investigations assuming the motion to be quasi-static have been studied by (Sera *et al.*, 2013; Perchiazzi *et al.*, 2014). By using a prospective cardiac gating technique, a spatial resolution of 1.1 μm was achievable in studying mouse lung motion necessitated by an integration time of just 3 ms (Lovric *et al.*, 2017). By changing the level of positive pressure at the airway opening, they were able to resolve alveolar structures at different levels of inflation. However, imaging the lung in static conditions is less physiological and does not allow capturing the full scope of local lung mechanics. This is due to lung tissue being viscoelastic, i.e. that its apparent elastic properties depend on the rate of the volume change (Suki and Bates, 2011). Several drawbacks make it useless for many practical applications where the motion, especially where fluid dynamics plays a significant role. Such is this case in our investigations. The only possible strategy to assess the dynamics of respiration is with retrospective gating.

A novel methodology, described in the work of (Mokso *et al.*, 2015) significantly improves the approach to capture the full dynamics, becoming restricted though to periodic motions. As the heart and respiratory cycles are quasi-periodic, a three-dimensional image can be obtained synchronizing the projections with specific phases across several, successive cycles of movement. The resulting tomograms, are a collection of averaged images, corresponding to numerous phases within multiple cycles of the heart and respiration. An imaging protocol was previously developed to respectively resolve cardiogenic motion combined with the mechanical ventilation (Fardin *et al.*, 2021).To avoid motion artefacts in the reconstructed images, mechanical ventilation and the heartbeat wave were synchronized by triggering the respiratory cycle with the R peaks of the ECG. This retrospective gating technique allows for dynamic measurements during the entire breathing cycle. This method was further developed to investigate regional lung acini and vascular strain during positive-pressure breaths and to assess conformational changes during positive pressure breaths in intact peripheral lung airspaces (Cercos-Pita *et al.*, 2022). One task performed in this work, was to apply the adapted technique by Cercos-Pita et al. to investigate how microscopic strain distribution in lung airspaces determines structural damage and inflammation, under mechanical ventilation in combination with early-stages of Bleomycin induced lung injury.

X-ray imaging

X-ray computed tomography (CT) refers to the cross-sectional imaging of an object obtained after irradiation with X-rays from multiple directions around the object. The importance of X-ray based CT, is that it is a non-invasive method which allows to view the morphology of an organ in three dimensions (3D), therefore avoiding the problem of superimposition of structures and the loss of information typical of projection techniques (2D), like planar x-ray radiography.

Micro-computed tomography (µCT)

CT is commonly used as a diagnostic tool in clinical routine examinations, as well as in preclinical studies on animal models. The CT systems used for small animal measurements do not differ, in principle, from the clinical systems. The main difference is the required higher resolution (spatial-, contrast- and temporal resolution). This is achieved by using micro-focus X-ray tubes with smaller focal spot sizes, typically between 1 to 50 µm, to create high-resolution images. Other notable differences are lower output power, smaller scanning fields, and relatively longer scanning times.

CT X-ray sources consist of an anode and a cathode. The cathode, part of the X-ray tube, expels electrons and focuses them on the focal spot of the anode. The most widespread type of X-ray source, typically in µCT systems for *in-vivo* imaging, produces electrons by heating a filament through thermionic emission, where a coil of tungsten wire releases electrons when heated. These electrons accelerate to considerable speeds (typically 30-65% of the speed of light) for medical applications (Krestel, 1990) and hit the anode, which produces the X-rays. The focal spot is where electrons hit the anode, emitting X-rays in all directions. The tube housing absorbs unnecessary X-ray radiation limiting leakage. Typically, tungsten are the chosen metal targets because of their high heat resistance and x-ray-generating properties. These so-called electron-impact X-ray sources, typically used in commercial systems utilize absorption-based X-ray imaging (in this specific case in the MILABS xUHR-µCT system).

The line focus principle utilizes the fact that the X-ray emission is non-Lambertian to increase the effective power load capacity by extending the targeted area but extending the apparent source area almost constantly by viewing the anode at an angle. This increases the attainable power load capability by up to ~10x. Further improvements were introduced in the 1930s to extend the effective electron-beam-heated area by rotating a cone-shaped anode to continuously provide a cool target surface and is still the state-of-the-art for most commercial µCT scanners.

Absorption-contrast imaging

In absorbed-based lung imaging, the differentiation between various tissue densities results in differing contrasts between air and different tissue densities within the lungs, such as between healthy tissue, fluid-filled areas or fibrotic regions. The X-rays generated in an electron-impact X-ray source spans a large energy range due to the continuous bremsstrahlung emission. The low-energy photons will have much lower transmission probabilities than the high-energy photons in the spectrum leading to unwanted radiation exposure. The low-energy X-rays do not contribute to image formation but only result in increase of the radiation absorbed dose, which is undesirable. When the X-ray beam passes through denser structures such as bones surrounding the lung tissue. This effect can lead to the misinterpretation of tissue density, as the 'hardened' beam may falsely represent the density of the underlying lung tissue. The solution to this problem is energy filtering of the X-rays, typically by using a few micrometres of aluminium to absorb a large portion of the low-energy photons. This approach not only reduces the patient's exposure but also minimizes the risk of beam hardening artefacts. The downside is that flux of X-rays decreases.

On the other hand, X-rays with too high energy will be absorbed to a very small extent and increase the background signal on the detector and, consequently, lowering the image contrast. Here the solution is not to have too high a voltage across the X-ray tube.

Index of refraction and synchrotron phase-contrast imaging

As an X-ray interacts with matter a phase change occurs due to coherent scattering. The amount of phase shift is determined by the refractive index, $n = 1 - \delta + i\beta$, of the matter. Where δ is the decrement of the real part of the refractive index responsible for the phase shift, and β is the imaginary term determining the absorption in the object, δ and β both depends on both the radiation wavelength, λ, the density, the atomic number and the atomic weight of the object.

As an electromagnetic wave interacts with an object the wavefront gets distorted due to different refractive indices at different positions along the wavefront. Large refractive index differences yield more distinct phase-shifting effects. The phase-contrast method employed in Study **II** is known as In-Line or Propagation-Based Phase-Contrast Imaging. PBI requires a sufficient degree of spatial coherence in the incident x-ray beam, which can effectively only be achieved at synchrotron light sources. The principle of PBI (Momose *et al.*, 1996) is based on a sufficient sample-to-detector distance allowing the refracted photons to interfere, thereby adding near-field interference patterns to the absorption image (Figure 1).

To generate X-rays from a synchrotron light source for propagation based phase-contrast imaging, electrons are initially produced using an electron gun, the electrons are accelerated into a linear accelerator that then boosts the electrons to higher energies using a series of oscillating electric fields within resonant cavities. After reaching, the desired energy, the electron beam is transferred to the synchrotron's storage ring, where it is maintained in a circular path by magnetic fields. Along this path, as the electrons are deflected by magnetic devices such as undulators and wigglers, they emit X-rays. The primary difference between wigglers and undulators lies in the motion of the charged particles in the transverse direction. In an undulator, the motion is set to be on the order of the characteristic opening angle of synchrotron radiation, resulting in coherent addition of radiation from different periods. This leads to sharp peaks at harmonics of the resonant frequency, which depends on the electron energy, undulation period, field strength, and observation position. In contrast, in a wiggler, the motion is made larger than the opening angle, leading to a broader spectrum of radiation.

The propagation-based method is the simplest way to image the phase information of an object, as the only requirements are a source with moderate spatial coherence, a sufficient flux to keep exposure times reasonable and some distance between the object and the detector. Such as in the following image:

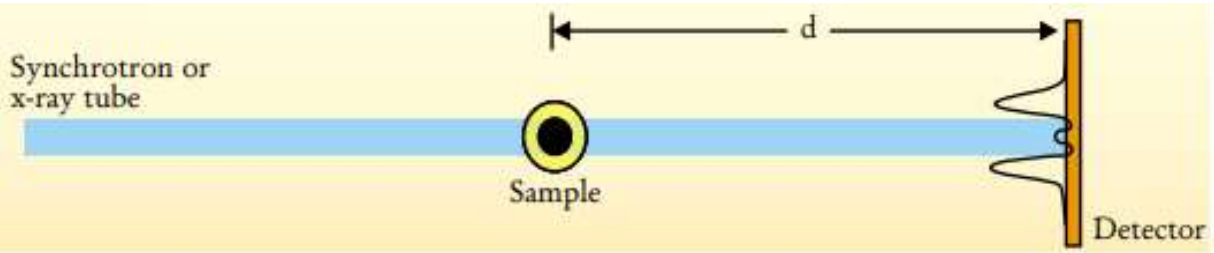

Figure 1. Experimental arrangement for propagation-based phase-contrast imaging. The detector is positioned at a distance far enough behind the sample so that the distortions in the wavefront caused by the sample result in the creation of interference fringes at the detector. When the distance between the object and its image, denoted as d, is optimal, these fringes lead to enhanced edges in the image. Adapted from (Fitzgerald, 2000).

Detectors in computed tomography

There is a close link to detector resolution and radiation absorbed dose.

Current CT detectors are made from complementary metal-oxide-semiconductor (CMOS) technology due to the advantages in X-ray imaging applications. Offering low power consumption, high-speed readout, on-chip integration and the ability to produce signals without external converters. In Study **I**, the CMOS detector integrated into the MILabs xUHR-µCT features an array that is 1536 x 1944 pixels, with a 14-bit digital X-ray camera with a pixel size of 75 µm. This array offers a field of view, capable of covering the entire lung of the animal but lacks the capability to visualize the alveolar scale of the acini. Whereas in Study **II**, the

synchrotron imaging equipment used a PCO Edge 5.5 CMOS detector with an array of 2560 x 2160 pixels and a significantly smaller pixel size of 6.5 μm.

This smaller pixel size is important to visualize the acinus at the alveolar scale, as higher spatial resolution is required than what is feasible with the detector in Study **I**. While magnification techniques and reconstruction algorithms can help to further increase the voxel resolution, it cannot overcome the inherent limitation imposed by the pixel size. This limitation is known as the Nyquist limit (Nyquist, 1928), which states that to accurately represent a signal (determined by the pixel size), the sampling frequency must be at least twice the frequency of the signal (object details).

These smaller pixels are required to distinguish the interference fringes caused by the wave propagation for propagation-based phase contrast. A challenge is related to the radiation exposure required, to maintain the same signal in the 75 μm pixel size, the necessary photon flux must increase be a factor of over 100 to achieve the same level of image detail as the 6.5 μm pixel size. At the same time, the detector's quantum efficiency decreases as the pixel size is smaller as the quantum efficiency is determined by the sensor's thickness, resulting in even higher radiation absorbed doses to the sample. Thus, a significantly higher flux of X-rays is required for smaller pixel sizes.

The X-ray sources in pre-clinical μCT scanners have significantly lower X-ray flux than synchrotrons. Though synchrotron radiation can provide lower radiation absorbed doses while giving similar image quality as preclinical μCT scanners (due to the ability of monochromatization). Synchrotrons can also significantly increase the spatial resolution because of the high X-ray flux.

Radiation dosimetry

A radiation dosemeter is a device that measures the quantities of the absorbed dose from ionizing radiation. It can be calibrated for different risk related quantities such as personal dose equivalent. Dosemeters often require to undergo some pre-processing before their signals are read out by a "reader" i.e. a system that can extract the information imparted onto the dosemeter as a result of exposure to ionizing radiation. Dosemeters are categorized as either active or passive. Active dosemeter systems require electrical power, while passive dosemeters do not. There are several sub-categories of both systems, but the two that will be of focus in this work are two types of luminescent solid-state dosemeters: namely thermo-luminescent dosemeters (TLD) and optically stimulated luminescent dosemters (OSLD). Luminescent solid-state dosemeters are made from crystalline materials that exhibit luminescent properties when exposed to ionizing radiation. The stored signal from the exposure can be read by exposing the sample to heat

(thermoluminescence) or light (OSL) and registering the luminescence photons with a photo multiplier tube (PMT).

The axial dose profile D(z) is commonly measured in clinical systems using an ionization chamber (Shope, Gagne and Johnson, 1981). The challenge with using this method for small animal systems is that ionization chambers are generally too large to obtain detailed dose information on the scale needed for these systems. However, the radiation absorbed dose can be measured discretely using TLD based on LiF (Figueroa *et al.*, 2008), metal oxide semiconductor field-effect transistor (MOSFET) (Bretin *et al.*, 2015) or OSLD based on Al_2O_3:C crystals (Vrigneaud *et al.*, 2013).

Microdosimetry for TLDs and OSLDs

Luminescence is radiation above the thermal radiation background caused by a transfer of electrons from an elevated energy state to the valence band. It is a two-stage process. First, the charge released in the crystal by ionizing radiation is captured in crystal lattice defects creating long-lived metastable trapping centres. Next, heating the crystal to a temperature of about 240°C to 300°C releases electrons which migrate to luminescence centres and lead to the emission of light which ideally is proportional to the absorbed dose. This process is called thermally stimulated luminescence (TSL) or simply thermoluminescence.

In the present project, it was also of interest to test a novel type of dosemeter as cost-effective and accessible OSL dosemeter, made of household salt (NaCl) in pellet form. NaCl pellets have been used in prospective and retrospective applications (Bernhardsson *et al.*, 2009; Spooner *et al.*, 2011; Ekendahl, Bulánek and Judas, 2016; Waldner and Bernhardsson, 2018; Bernhardsson, Waldner and Vodovatov, 2017; Waldner, Rääf and Bernhardsson, 2020), and medical dosimetry applications (Solak, 2021) but not in pre-clinical applications. Though other OSLDs have previously been applied in small animal diagnostic dosimetry applications (Vrigneaud *et al.*, 2013; Mendez *et al.*, 2018), TLDs have also been widely used in small-animal dosimetry applications (Carlson *et al.*, 2007; Willekens *et al.*, 2010; Figueroa *et al.*, 2008; Hupfer *et al.*, 2012). While these studies applied various TLD types, the specific MCP-N (LiF:Mg,Cu,P) TLD from TLD Poland (now RadPro International Gmbh) used in this work has not been used for determining the radiation absorbed dose to small animals.

Small-animal *in-vivo* dosimetry

In preclinical research with μCT, it is important to understand and quantify the radiation absorbed dose delivered during imaging to minimize the risk of harmful effects on the animals (Clark and Badea, 2014). As the total absorbed radiation

absorbed dose is a function of radiation exposure, beam hardness, and desired image quality (resolution, noise, contrast). The pre-clinical μCT radiation absorbed doses are typically in the range from 35 – 700 mGy, depending on the μCT imaging protocol used (Carlson *et al.*, 2007; Berghen *et al.*, 2019). There are fundamental limitations to the spatial resolution achievable for longitudinal *in-vivo* pulmonary imaging studies (Ford, Thornton and Holdsworth, 2003). There is literature to support that the lung parenchyma can sustain as high as 5 Gy of radiation absorbed doses accumulated over 6 weeks (Detombe *et al.*, 2013), specifically from X-ray energies typically in diagnostic energy range. However, if the intended research goal is to investigate the mechanics and function of the alveolar acinus, this requires a spatial resolution of less than 10 microns to visualize the alveoli septa. The total radiation absorbed dose reaches levels that are not applicable for longitudinal *in-vivo* investigation. With future advancements, this may be become possible (Albers *et al.*, 2023). The intention of Study **I** was to investigate radiation absorbed dose levels as experienced in routine lung imaging studies not intended to investigate the alveoli micromechanics, as is the case in Study **II**.

Ventilator-induced lung injury (VILI) and acute respiratory distress (ARDS)

CT of the lungs is considered the gold standard for assessing heterogeneous lung injury, showing the first time the regional distribution of aeration (Gattinoni *et al.*, 2001). Lung fibrosis is a disease with high mortality and few treatment options with a mortality of about 40%, with a incidence about 500.000 persons/year in the European Union (Bellani *et al.*, 2016a). The challenge is thought that ventilation strategies fail due to the remaining gaps in our understanding of lung deformation at the acinar scale. Directly visualizing and quantifying the regional distribution at the acinar scale of the lungs. Has only recently been achieved in mechanically ventilated studies (Cercos-Pita *et al.*, 2022) and has not yet been achieved in spontaneous breathing.

Mechanical ventilation (MV) is a vital therapeutic modality that facilitates alveolar gas exchange by mechanically augmenting or supplanting pulmonary ventilation in patients with ARDS. Ventilatory support was first introduced during the polio epidemic in Copenhagen 1952. An iatrogenic complication to MV, known as VILI affects the alveolar micromechanics (Bates and Smith, 2018) and is exacerbated by ARDS, defined by the Berlin Definition (Ranieri *et al.*, 2012). The pathogenesis of VILI is associated with the biomechanical stressors imposed upon the pulmonary alveoli. Where a phenomenon of alveolar over-distension, termed volutrauma (Webb and Tierney, 1974; Hernandez *et al.*, 1989) and the recurrent alveolar collapse and re-expansion, known as atelectrauma (Muscedere *et al.*, 1994), both directly disrupt the homeostatic alveolar mechanical forces (Smith *et al.*, 2020). The

mechanical properties of pressure-controlled ventilators, notably tidal volume and Positive End-Expiratory Pressure (PEEP) modulate the extent of these microscale injuries. While PEEP is instrumental in sustaining alveolar recruitment, it simultaneously possesses the potential to induce alveolar over-distension. This balance becomes increasingly difficult in pathological states such as ARDS, where the reduced lung compliance increases the susceptibility to VILI consequent to the altered mechanical properties of the lung (Nieman *et al.*, 2023).

At the alveolar level, the ramifications of VILI are multifaceted, encompassing the disruption of the alveolar-capillary interface and the initiation of an inflammatory cascade, which collectively exacerbate the pulmonary condition, particularly in ARDS as exemplified by Knudsen et. al. (Knudsen *et al.*, 2018). Thus, a profound understanding of the impact of MV on alveolar micromechanics is imperative for management of VILI. As the mechanistic understanding of different ventilation strategies would enable to minimize alveolar strain and optimize lung compliance. One specific aim of this research was to identify an appropriate ventilation strategy, which provides life support while minimizing the progression of the injury and reducing mortality.

Animal models of ARDS and PF have been used to explore pathological processes and early development as clinical presentation generally is not diagnosed until later stages of disease progression (Brass *et. al.*, 2007). Several PF models have been investigated (Ye *et. al.,* 2023). To summarize, the more commonly used models include asbestos, bleomycin and adenovirus vectors (B. Moore *et al.*, 2013). Each model differs in their induction and results in different pathological features. The method to induce ARDS used in Study **II** is known as a drug-induced interstitial lung disease (DILD). The reference model for lung injury research has been completed by a single-dose by intra-tracheal instillation of bleomycin. In rodents, the early phase (3 to 7 days) induces lung inflammation injury that shares many features with ARDS including neutrophilic infiltration, high-permeability edema and extensive alveolar micro-atelectasis that are followed by a later fibrogenic stage (Matute-Bello, Frevert and Martin, 2008). These changes drastically modify the extracellular matrix (ECM) structure and the macroscopic tissue viscoelastic behavior (Knudsen *et al.*, 2018).

Global lung mechanics

The relationship between global lung deformation and ARDS is significant, as ARDS is characterized by reduced lung volumes and compliance, which are key physiological abnormalities in the condition (Henderson *et al.*, 2017). Global mechanical measures such as lung compliance are still more routinely used to indicate the likelihood of a given pathology. Understanding global lung deformation is crucial in the context of ARDS, as it influences the design of safer approaches to

setting the ventilator and the management of pulmonary stress-strain relationships in severe ARDS (Hubmayr and Kallet, 2018). The decrease in lung compliance in ARDS is attributed to the reduction of airspace volume due to alveolar fluid and superimposed pressure, along with impairment of surfactant function (Russotto, Bellani and Foti, 2018). The concept of the "baby lung" in ARDS, which refers to the reduction of lung compliance and the presence of atelectatic and edematous airspaces, underscores the importance of global lung deformation in the pathophysiology of the condition (Nieman *et al.*, 2022). The shrinking of the "baby lung" and the associated reduction in lung compliance are central to the development of ARDS and its management. Therefore, global lung deformation is a fundamental aspect of ARDS, influencing both its pathophysiology and the design of ventilation strategies.

In the study of lung mechanics, specifically in ARDS patient care, measuring lung mechanics through static and dynamic lung compliance indirectly reveals alveolar changes. Decreased lung compliance, determined via lung pressure-volume curves or the Forced Oscillation technique (LFOT), indirectly investigates alveolar issues like reduced Functional Residual Capacity due to lung collapse (atelectasis) and fluid buildup (edema). These compliance changes, reflecting the lung's ability to expand, indirectly signify alterations in the alveoli. Although these measurements are crucial for understanding the conditions of ARDS and VILI, they are averaged over the whole chest-lung system. As a consequence, they do not provide direct information on the phenomena acting at the alveolar scale and they cannot be used to study the mechanistic link between overdistension and atelectrauma and the inflammatory response as the spatial distribution of ARDS and VILI are highly regional and heterogeneous.

Methods

Paper I Dosimetry study

MILABS xUHR µCT

To initially benchmark the dosimetry results from the TLDs, we wished to compare our measurement values with the vendor-provided dose values for the systems pre-defined imaging scans/protocols. For each of MILabs xUHR-µCT pre-defined imaging protocols there are pre-determined doses. One aim with the first study was to compare these doses with TLD and OSLD measured using a PMMA phantom.

MILABS offers the user to seamlessly switch between "whole-body" and "ultra-focus" field of view modes to reduce the distance between the object and the X-ray source. The system is equipped with one X-ray filter that is non-interchangeable consisting of 100 µm Al, while three X-ray filters are interchangeable in the software, (i.e. 250 µm Al, 400 µm Al, 200 µm Cu). The three interchangeable filters can be combined with the 100 µm Al filter, if desirable, for energy filtering of the X-ray beam.

All µCT scans were performed at Lund University Bioimaging Centre (LBIC), Lund University, Lund, Sweden in the MILabs xUHR-µCT system. MILabs advertises to be unrivalled in *in-vivo* dose efficiency, compared to other conventional µCT scanners, offering whole-body scans down to 2 mGy (Table 1). The vendor offers scanning beds that scale up to fit mice, rats, ferrets and rabbits and are made of PMMA. The acquisition software has a collection of "default" imaging protocols that offer optimized parameters for the most common applications. The default protocols include four basic parameters, magnification, scan angle, voltage and scan mode. The magnification allows for movement of the X-ray tube towards the subject to obtain a larger magnification and therefore higher resolution (as well as higher dose). The scan angle can be defined as either partial (220°) or full (360°) rotation of the CT gantry. The voltage in the X-ray tube can be varied between 20 and to 65 kVp.

The scan mode provides combinations of binning, step angle (available in step-and-shoot mode), and rotational speed (continuous mode) of the gantry; it also allows acquisition with retrospective gating. The four default scan modes are: Fast,

Normal, Accurate and Gated. The system provides an estimated dose value for the default settings. The settings and dose values are found in Table 2. The Fast protocol allows short scans using continuous rotation. The Normal and Accurate protocols are step-and-shoot modes that yield improved image resolution and quality but also an increase of the scan time, radiation absorbed dose and reconstruction time. In the Accurate protocol, more angular projections are acquired than in the Normal protocol. The Gated protocol allows for respiratory and/or cardiac gating, as well as one additional gating signal source. It is also possible to adjust parameters as needed and set up your own custom protocols.

This became of interest as it is left up to the user(s) to devise their procedures to estimate the dose delivered to their animals. This further leads to several potential research questions that can be addressed for *in-vivo* imaging applications.

1) What dosimetry methods are best applicable to accurately assess the dose to an animal in the MILabs scanner?
2) What is the highest image quality achievable while maintaining a "translatable" dose compared to clinical scanners?
3) Specific to retrospectively gated lung imaging, what are the most optimal settings for imaging protocols for end-expiration and 4DCT imaging?

To the best of my knowledge, nothing has been reported in the literature addressing these potential research questions for the MILabs μCT. We addressed the first question in this work.

To initially benchmark the dosimetry results from the LiF chips and NaCl pellets, we compared our measurement values with the vendor-provided dose values for the four default imaging protocols (Table 2).

Table 1. Properties of MILabs xUHR-µCT scanner. Table from paper 1.

X-ray tube	Sealed air-cooled, tungsten anode
Focal spot	7 µm
Power	12 W
X-ray detector	CMOS 1536 x 1944, 14-bit digital X-ray camera with 75 µm pixel size
CT-zoom turned on	Yes
Continuous scan mode	Yes
Step-and-shoot mode	Yes
Rat bed	Ø60 mm x 230 mm
Highest spatial resolution, MTF @ 10%	14 µm
Max tube voltage	66 kVp
Max tube current	0.26 mA
Gating	Extrinsic retrospective respiratory and cardiac gating
Live-view X-ray CT images during acquisition	Yes
Radiation safety	< 1 µSv/h at any place surrounding the instrument

Table 2. Protocol settings for the various standard imaging protocols of the µCT scanner. Table from paper 1.

Protocol Settings	FAST	NORMAL	ACCURATE	GATED
Tube voltage [kVp]	55	55	55	55
Tube current [mA]	0.17	0.17	0.17	0.17
Exposure time per projection [ms]	20	75	75	20
mAs	0.0034	0.01275	0.01275	0.0034
Total exposure time [s]	7.2	72	108	153.6
Scan mode	Continuous	Step-and-shoot	Step-and-shoot	Step-and-shoot
Step angle	N/A	0.375	0.25	0.75
Projections per step	N/A	1	3	16
Number of projections	360	960	1440	7680
Filters	500 µm Al	500 µm Al	500 µm Al	500 µm Al
Vendor provided absorbed dose [mGy]	13	299	420	673

Absorbed dose measurements

An OSL material made from ordinary household salt (NaCl) was used to investigate if this alternative could be implemented for small-animal dosimetry diagnostic studies. The NaCl grains were compressed into a pellet form (Waldner, Rääf and Bernhardsson, 2020) , for easier handling and signal integrity.

All LiF chips and NaCl pellets readout were readout using Risø TL/OSL readers (TL/OSL-DA-15 and DA-20, DTU Physics, Denmark) at Lund luminescence centre

for dosimetry at the medical radiation physics group in Malmö (www.msf-malmo.lu.se/lund-luminescence-laboratory-dosimetry-llldo-lab). The components of the readers include:

1. A carousel for sample cups,
2. Stimulation light sources,
3. A $^{90}Sr/^{90}Y$ calibration source (beta source)
4. A heating element
5. A photo-multiplier tube (PMT)

The samples are positioned on stainless steel cups, and these cups are placed on a removable sample carousel capable of accommodating up to 48 cups. Each sample cup can undergo heating, irradiation, and optical stimulation independently. The heating element also serves as a mechanism to raise the sample toward the Photomultiplier tube (PMT) to enhance the collection of light for optimal reading efficiency.

For TL stimulation, the heater/lift gradually increases in temperature while the PMT records the luminescent photons emitted. In the case of OSL stimulation, blue LED lights are used to illuminate the sample, and the PMT registers the luminescent signal. The PMT is equipped with a Hoya U-340 filter to eliminate scattered light from the stimulation process when blue stimulation is used.

The internal calibration source ($^{90}Sr/^{90}Y$) emits beta particles with a maximum energy of 2.27 MeV. The activity of the sources can be adjusted to suit the specific area of application or research (DA-15 source has a dose rate of approximately 0.5 mGy/s whereas DA-20 is approximately 4 mGy/s). Quartz is commonly employed as a standard material to calibrate the radiation source and determine the current dose rate. The current calibration quartz is pre-irradiated at DTU Nutech (Hansen *et al.*, 2015).

Readout protocols

The read-out process for the TLDs on the DA-15 reader is as follows:

Table 3: TL readout settings for the LiF chips.

Step	Operation and readout settings
1.	Anneal TLDs in oven at 240°C for 10 minutes to remove any residual signal
2.	Administration of the unknown dose, Du
3.	Anneal TLDs in oven at 100°C for 10 minutes before read-out
4.	Read-out at Su at ambient temperature

The read-out process for the OSLDs on the DA-20 reader is as follows:

Table 4: OSL readout settings for the NaCl pellets.

Step	Operation and readout settings
1.	Administration of the unknown dose, Du
2.	Pause for 1 hour
3.	Read-out at Su at ambient temperature, continuous OSL at 40% (~16 mW cm-2) of maximum blue (λ=470±30 nm) LED intensity during 20 seconds
4.	Administration of a calibration dose, Dc, using the internal 90Sr/90Y source
5.	Pause for 1 hour
6.	Readout of Sc at ambient temperature, OSL at 40% of maximum blue LED intensity for 20 seconds

Absorbed dose estimation

The PMMA phantom was positioned in the iso-centre of the rat bed. A source to detector distance (SDD) was recorded by the vendor software to 297.8 mm and the source to iso-centre distance (SID) of 119.4 mm was constant throughout all measurements (Ultra Focus). All μCT settings for the imaging protocols are provided in Table 2. Two different dosemeter materials and readout methods were used to quantify the absorbed doses in the PMMA phantom. TLDs were used as reference dosemeters and in parallel, OSLDs based on NaCl were studied for the potential use of the present purpose. For each combination of exposure settings (each imaging protocol), six individual measurements were performed with LiF chips and NaCl pellets, respectively, positioned in the phantom Fig. 3. The radiation absorbed doses were calculated as the arithmetic mean of the results from the six exposures. The agreement between the dose assessments using the TLDs and the OSLDs was determined as the difference between the corresponding read-outs to decide whether whether the mean difference was significantly different from zero. A two-sided one-sample t-test was used.

TLD dose estimation procedure:

The individual TLD chips were calibrated at Skåne University Hospital in a ^{60}Co beam. A reference dose of 100 mGy was delivered and read out repeatedly until the luminescence signal from the calibration converged to the same signal within 5%. The dose was verified by using a PTW semiflex 31013 ionization chamber (PTW-Freiburg, Freiburg, Germany) that was positioned in a standard PMMA (30x30x15 cm^3) calibration phantom. This provided a well-defined dose rate at the position of the phantom. At the same location in the phantom the TLDs were positioned and irradiated. All irradiations occurred within a four-hour window from the annealing (Table 3). The uncertainty in energy dependence was stated to be less than less than 20% for photon energies between 30 keV – 1.3 MeV. Among the 100 TLDs that

were calibrated, 24 selected as best having the lowest signal differences. Readout of the TL signals was performed using a linear heating rate of 5°C s^{-1} up to 240°C, after which the temperature was held constant for 60s to assure a high depletion efficiency of the signal (Table 3). The uncertainty of the absorbed dose to water by means of TL in LiF is estimated as below 5% based on data presented by (Shen *et al.*, 2002).

OSL dose estimation procedure:

Using a stopping-power ratio of 0.938 between NaCl and SiO_2 the $^{90}Sr/^{90}Y$ dose rate to a thin layer of NaCl corresponds to 0.5772 mGy s^{-1}. After exposure of the NaCl pellets in the μCT, they were read out the day after and were individually calibrated using the internal $^{90}Sr/^{90}Y$ of the reader (Table 4). By using a calibration dose with similar magnitude as the dose from the μCT, this calibration procedure provides a reproducibility of <2% (Waldner and Bernhardsson, 2018). Each NaCl pellet was used only once. An energy dependence correction of 14 (D_{NaCl}/k_{air}) was applied for a mean energy of approximately 30.0 keV that was determined using an open access software (SpekCalc) to estimate the average energy fo the X-ray beam spectrum (Poludniowski *et al.*, 2009).

Phantom development

Dosimetric phantoms are used for various purposes, e.g. for establishing absorbed-dose distributions in irradiated patients. In Study **I**, this is further extended to small animals. In order to resemble the radiation attenuation in tissue water equivalent materials are used to make such phantoms (White *et al.*, 1992). The American Association of Physicists in Medicine (AAPM) established polymethyl methacrylate (PMMA) as a phantom material for CT dose measurements (Dixon, Anderson and Bakalyar, 2010). PMMA is commonly used x-ray phantom and is approximately tissue equivalent with a density of about 1.19, compared to water with a density of 1.0.

The PMMA phantom for all dosimetry measurements was designed and tailored in-house, manufactured and authored by Promech Lab AB, (Promech, Sweden). The phantom was designed to resemble the size of a mature rat and adopted to fit the bed of the μCT scanner (total length of 50 mm). In the cylindrical phantom four bore holes spaced 10 mm apart (Fig. 3a), were constructed. The depth between each such hole was determined to 6.13 mm in-depth, resembling different tissue depths in the animal (Fig. 3b).

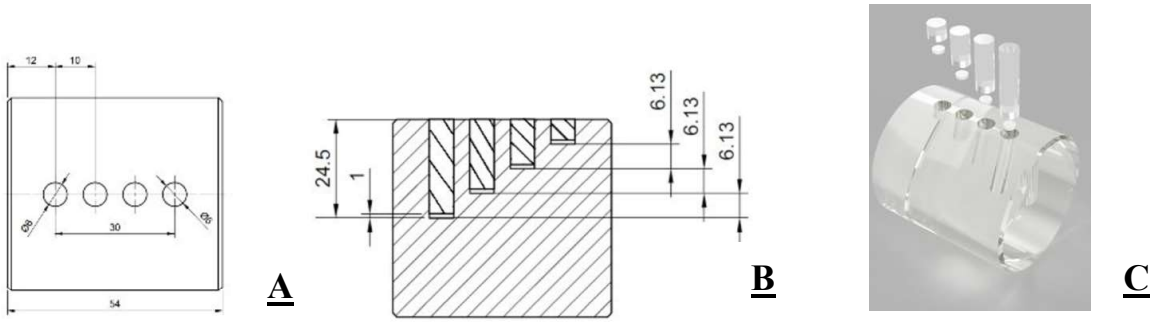

Figure 3. Schematic outline of the PMMA phantom. (a) A top view angle (b) Cross-section of the phantom from the side, showing the depths of the four dosemeter slots. (c) Volume rendered PMMA phantom, flute design, with four bour holes at separate depths of 6.13 mm difference from the iso-centre towards the surface.

A computer-rendered image of the phantom with example dosemeters is shown in **Figure 3**.

Paper II: Synchrotron measurements

The biomedical beam-line ID17 at the European Synchrotron Radiation Facility in Grenoble, France is one of the few beamlines at ESRF that gives the possibility to create a source-to-detector distance of 160 meters. It contains two experimental stations, the first is primarily used for microbeam radiation therapy experiments (Bräuer-Krisch *et al.*, 2005) and the second experimental station known as the "monochromatic imaging" station. The monochromatic imaging station is 140 meters long and has been used extensively in preclinical investigation for lung imaging (Broche *et al.*, 2017; Porra *et al.*, 2017). A general description of the beamline can be found in Elleaume et al. (Elleaume *et al.*, 1999).

The monochromator used is a double bent-Laue crystal (Elleaume *et al.*, 1999). It consists of two Si(111) cylindrically bent asymmetric crystals, with an asymmetry angle of 15° and a thickness of 1 mm. The advantage of this is that it allows for fine-tuning to increase the flux available at the sample position and improves the stability of the beam, producing a stable monochromatic beam in the range of 25 keV – 150 keV, with a bandwidth of 0.1% (Suortti and Schulze, 1995). and a maximum size of 150 mm x 10 mm. Inside the experimental station's hutch, a rotation stage is used to place animals for tomographic experiments, and a system of beam shutters which can stop the irradiation to avoid unnecessary exposure to animals and detectors.

Detector system

For *in-vivo* imaging, the most stringent requirement is to acquire projections fast, in order to neglect motion during the detector integration time. The detector employed to ensure this is the PCO Edge 5.5 camera, an air-cooled CMOS image sensor (Fairchild Semiconductor, Sunnyvale, California, USA), with a physical pixel size of 6.5 µm and composed of an array of 2560 x 2180 pixels, corresponding to an active area of (16.6 x 14.2) mm^2. With a 16-bit dynamic range and operated in "rolling shutter" mode.

In the rolling shutter modality, the pixels in each row start and reset, row by row (Mittone *et al.*, 2017). Meaning that different rows are exposed during different time intervals, starting from the outside towards the centre. This is the fastest imaging modality but can introduce distortions in the image for moving objects. The time shift between rows is 10 µs, which results in a maximum delay which is negligible for our study. The maximum frame rate in rolling shutter mode is 100 fps at full frame rate. To increase this, a reduction of the field of view was performed. To achieve a frame rate of 333 frames per second (fps), the field of view was reduced to 2374 x 291 pixels to correspond to an active area of 15.4 x 1.9 mm^2. The camera is connected to the ESRF central storage server through a 10 Gb network. This transfer speed of the network also provides a limit to the maximum frame rate achievable with which data from the camera is transferred and saved on the ESRF server.

Optics and scintillators

The detectors are coupled to a system of scintillators and optical lenses. The scintillator employed for this experiment was a 250 µm thick Cerium-doped Lutetium Aluminum Garnet (LuAG:Ce) scintillator. The effective pixel size on the image varies with the distance between the sample and detector, due to the divergence of the beam. For the experiment in this work, the optics coupled allowed for an isotropic pixel size of 6 µm.

Translation and rotation stage

A moveable stage based on a tower of motors, whose specifications can be found in Mittone et al. (Mittone *et al.*, 2017) and which are shown in Figure 4.

- Horizontal and vertical translation: to position the sample in the laminar beam.
- Tilt axis: to align the plane of rotation and the camera.
- Rotation: an air bearing rotary stage RT150s from Lab Motion System. Maximum speed 200 rpm, angulary accuracy: 0.002°.

- Precise horizontal translation: for the fine positioning the sample inside the field of view.

Figure 4. Movable tomography setup at ID17. Adapted from (Mittone *et al.*, 2017).

Acquisition protocol during mechanical ventilation

For *in-vivo* imaging, the surgery typically consisted of a tracheostomy with the insertion of a catheter in the trachea, which allowed to connect the animal to a mechanical ventilator. In our experiments, we used a custom-made ventilator (Porra *et al.*, 2004), see Figure 5. A T-tube with an inspiratory and expiratory branch was supplied by air and oxygen bottles to control the fraction of inspired oxygen F_{IO_2}. The expiratory branch was connected to a column of water or to an adjustable positive pressure valve, to adjust the PEEP. The ventilator was

remotely controlled, allowing to set the inspiratory and expiratory time and gas flow. This was obtained by acting on an electromagnetic valve, placed on the expiratory branch: the valve was closed during inspiration and opened during expiration. The gas flow in the inspiratory branch, measured using a pneumotachometer (PNT) was adjusted manually. Therefore, no intervention was possible during imaging. The ECG signal, arterial pressure, airway pressure at the trachea (tracheal pressure, P_{TRACH}) and flow at the trachea were recorded using a Powerlab 16/35 data acquisition device (DAQ, Adinstruments, Dunedin, New Zealand) coupled with a BioAmp and Bridge Amps modules (Adinstruments, Dunedin, New Zealand). The signals were sampled at 10 kHz.

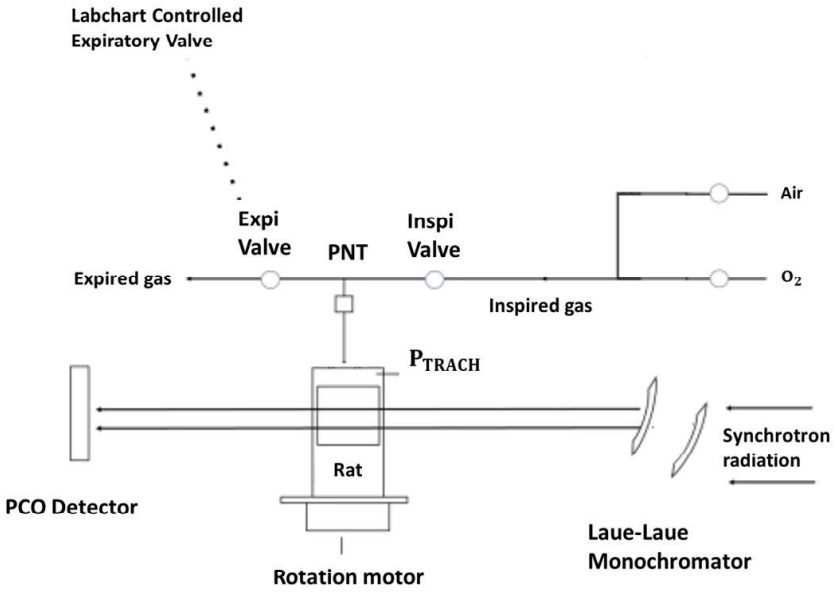

Figure 5. Scheme of the experimental setup for a conventional *in-vivo* lung imaging experiment. The animal is immobilized in a plastic holder and placed on the rotation stage. Adapted from: (Fardin, 2019)

A tomographic scan was acquired during a single slow half-rotation as the animal rotated, for 180° coverage. A constant angular velocity of $\omega = 0.34°\ s^{-1}$ was set to include approximately 700 respiratory cycles per scan. The speed of rotation of the stage was set to obtain approximately 1.000 periods of the heartbeat. An average heart cycle of 300-350 ms in the anesthetized rat determined a total scan duration of approximately 9 minutes, corresponding to 180.000 projections. The exposure for a single projection was set to 2 ms as a compromise between the signal to noise ratio (SNR) and time resolution; the delay between two exposures was set to 1 ms: the time interval between the start of the exposure of consecutive projections was therefore of 3 ms, resulting in 333 fps. The justification for a latency time was to provide a safety margin for motor speed fluctuations. Allowing for the system to acquire data at evenly spaced angles. This high time resolution and large number of projections was necessary to prevent under-sampling artefacts and low SNR ratio. If the motion is periodic, the number of projections acquired per phase is equal to the number of periods covered by the rotation. The duration of the scan was determined by the period of the motion and by the number of projections required for CT reconstruction.

In our experiment, $n_{vivo} \sim 700$, while $n_{sampling} \sim 80$. Where $n_{sampling}$ is the number of reconstructed time instants. On the other hand, n_{vivo} is the number of projections available to reconstruct each time instant. Due to the Filtered Back-Projection reconstruction, there is not a straight forward relation between n_{vivo} and the final spatial resolution and quality. The larger n_{vivo} is will result in enhanced quality of the reconstructed image, provided that the periodic *in-vivo* motion is not altered during the imaging acquisition. To implement this, the algorithm computes the

appropriate projections from the whole set of acquired images, based on the acquired cardiac and respiration signals from the mechanical ventilator from the Labchart software.

Mechanical ventilation in this study, used the airway pressure as a physiological signal represented by the tracheal pressure. The acquisition scheme was based on obtaining the best approximation of periodic motion of the lung parenchyma (Figure 7). Two sources of motion from the heartbeats and the mechanical ventilation influence each other but are not synchronized. To synchronize between the heartbeats and the mechanical ventilation every inspiratory-expiratory cycle was triggered with the ECG, specifically when an R peak was detected. The ECG acquired during the scan was analysed with a Matlab script (version 2017a, www.mathworks.com), to identify the QRS complexes based on the approach described in (https://se.mathworks.com/help/wavelet/ug/r-wave-detection-in-the-ecg.html). This method utilizes band-pass filtering within the wavelet domain to identify QRS complexes. Following the identification of these complexes, the detection's accuracy was assessed by calculating the time intervals between successive complexes. These intervals, which represent the duration of heartbeats, are anticipated to remain consistent or change gradually. If incorrect identifications of QRS complexes occurred, the band-pass filter's window within the wavelet domain was empirically corrected.

LabChart allowed to monitor the ECG, detecting R waves based on a threshold on the ECG signal. When an R wave was detected a square wave was generated, with a user-defined duration and duty cycle. The square wave was transmitted via a TTL signal generated by the PowerLab to the electromagnetic valve in the expiratory branch, controlling its status (closed-opened) and therefore the inspiration/expiration time. The ECG polling was disabled for the whole duration of the square wave, a concept equivalent to the busy signal of the mechanical ventilator as seen in Figure 7.

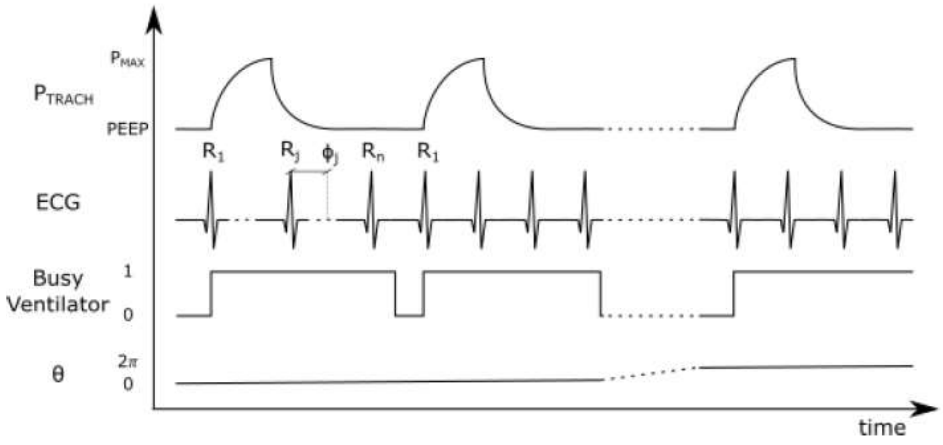

Figure 6. Scheme of the dynamic CT with mechanical ventilation. A respiratory cycle is triggered by the R peak of the ECG. Adapted from: (Fardin, 2019)

The most appropriate projection candidates were selected based upon, the candidates at each heartbeat, for a specific delay, t*. A local time window, $\Delta t^* > T_{cam}$, is defined in such a way that the projection candidates are those captured within the time window,

$$t_i + t* - \Delta T_{cam} < t < t_i + t* + \Delta t^*,$$

With t_i the time stamp of an arbitrary i-th heartbeat. Which marked a phase of parenchymal motion in the respiratory cycle, were used for reconstructing the image of that specific phase. The duration of the cardiac cycle is of approximately 300-350 ms, after which the new R wave starts, therefore the frames are almost monospaced. If the cardiac cycle was longer than 375 ms, then a third phase was reconstructed per heart period, positioned at 300 ms from the R peak.

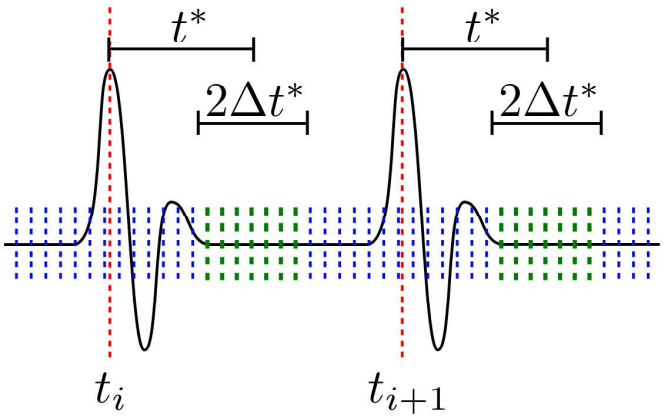

Figure 7: Visual depiction of the peak of the R-wave, where the red dashed lines depict the time instants sleected as the heartbeat triggering marks, while the blue dashed lines are the neglected projections time instants and the green dashed lines are the selected projection time instants. (adopted from personal communication with Jose-Luis Cercos-Pita).

The first step to registering the key time stamps, associated to the heartbeats and the camera snapshots. The second considers a new signal that is appended to the set of signals, which is the ventilation triggering function. This function fulfils the following criteria:

- The new signal is synced with the ECG, i.e. the ventilation is always triggered at the same time instant of an arbitrary ECG pulse.
- The ventilation trigger is a duration of approximately one second

Thus, the ventilation is triggered when an ECG pulse is detected, carrying out a whole ventilation cycle. After the imposed latency (~1 s) the systems recovers the initial state, and wait for a new ECG pulse to trigger the ventilation again. The number of ECGs within each ventilation period is not enforced, and therefore an irregular ECG profile would result in ventilation cycles with a different number of

ECG pulses. All the ventilation cycles with a different number of inner ECGs are neglected to avoid motion artefacts resulting from non-constant periods see Figure 8.

Resulting scans were acquired at 6 µm isotropic voxel size. See Figure for complete 3D microscopy imaging setup. With a temporal resolution of 10 ms time interval over one breath cycle with an average periodicity lasting between 740 ± 10 ms. Specifically, healthy controls had a periodicity of 780 ± 11 ms, while injured had a periodicity of 720 ± 8 ms. Ultimately, reconstructing between 72-78 successive time points within a single breath.

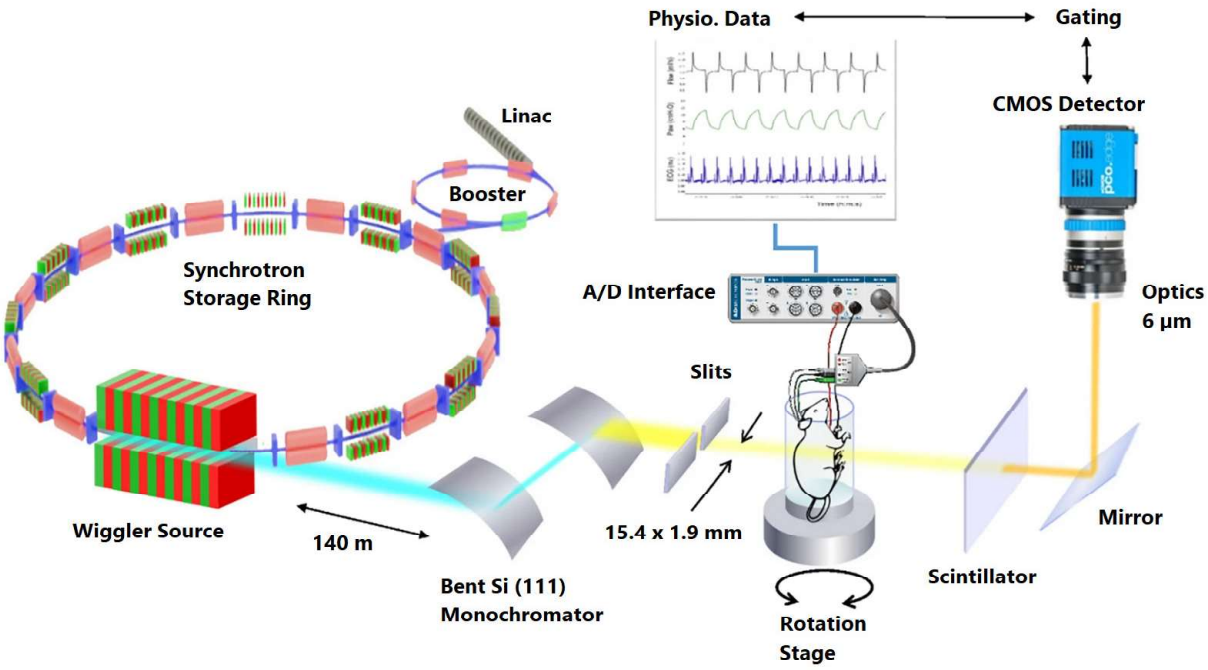

Figure 8: Dynamic 3D microscopy of a rat's thoractic cavity using ESRF's synchrotron X-ray source at ID-17 beamline. High-intensity coherent X-rays generated from electrons orbiting in a storage ring, are rendered monochromatic using bent silicon crystal optics, and detected by a PCO Edge 5.5 camera coupled to a Cerium-doped Lutetium Aluminium Garnet (LuAG:Ce) scintillator and optics yielding an isotropic pixel size of 6 µm. The anesthetized rat is mechanically ventilated while the electrocardiogram and respiration rate are monitored and recorded using Powerlab equipment and Labchart software. Adapted and modified from: (Cercos-Pita *et al.*, 2022)

Animal preparation and injury model

Procedure of bleomycin-induced ARDS model

The animals were anesthetized by inhaling 4% isoflurane, administered in a Plexiglas box provided for this purpose. After the induction, the animal was installed in dorsal decubitus on a sloped Plexiglas board. A polyethylene catheter (14 G) was placed in the trachea in inspiration, through the vocal cords visualized with a cold light applied to the neck of the animal. The location was checked using a pneumotachograph, showing a respiratory flow. Bleomycin (1000 IU in 200 µl of physiological serum) was instilled as a bolus through the cannula in inspiration, and purged with air. The animal was then placed in an incubator and monitored until it woke up. Control animals underwent a physiological serum instillation (200 µl) only. The animals were then monitored by daily for 7 days until imaging.

Procedure of FOT measurements

The low-frequency forced oscillation technique (LFOT) was employed to analyze the respiratory system's impedance, distinguishing between airway and lung tissue effects. Initially, two deep breaths inflated the lungs to 30 cm H2O. During a pause in mechanical ventilation at end-expiration, a small amplitude oscillatory force (1 cm H2O peak-to-peak) was applied via a loudspeaker system connected to the trachea. This system emitted a computer-generated signal ranging from 0.5 to 21 Hz, with measurements taken at a standard PEEP of 5 cmH2O. Pressure measurements at both ends of a connecting tube were filtered and digitized.

Using these measurements, the pressure transfer function (P1/P2) was determined through fast Fourier transformation, leading to the calculation of the respiratory system's input impedance (Zrs) based on transmission line theory. This calculation involved factors like the tube's length, its characteristic impedance (Z0), and the complex wave number (γ), integrating both the tube's physical properties and the gas within.

The impedance data, averaged over several measurements, was then fitted to a model accounting for airway resistance (Raw), inertance (Iaw), and lung tissue properties: damping (G) and elastance (H). Hysterisitivity (η), the ratio of tissue damping to elastance (G/H), was also calculated. Data affected by heart rate interference was excluded to maintain accuracy.

Procedure to obtain synchrotron X-ray tomography imaging data

Animals were anesthetized by inhaling 4% isoflurane, administered in a Plexiglas box provided for this purpose. After induction, the anesthesia was maintained by the isoflurane inhaled at 1.4% or 1 MAC, by nasal mask. After checking the depth of the anesthesia, the animal was tracheotomized while respecting asepsis, with a paediatric catheter (14-gauge, Brauna, Melsungen, Germany) and placed under protective mechanical ventilation. Protective mechanical ventilation was induced (tidal volume=10 ml/kg body weight; inhaled fraction of O_2=0.5; maximum tracheal pressure=30 cmH_2O), and a respiratory rate of 70-80 cycles per minute, using a custom mechanical rodent ventilator, as described in the protocol on acquistion (as described. A positive end-of-expiration pressure (PEEP) of 5 cm H_2O was applied depending on the needs of the experiment. Anesthesia was continued by Ketamine 80-100 mg/kg and xylazine 10-12.5 mg/kg by intraperitoneally (surgical preparation, then inhaled with isoflurane 2% by the tracheal tube, once the animal was installed on the imaging platform. The intratracheal pressure was recorded continuously using a calibrated sensor, as well as the ventilatory flow rates. A catheter (26-gauge, Braune, Melsungen, Germany) was placed in the carotid artery to monitor blood pressure and collect 0.1 ml of blood to analyze the gases of the arterial blood. A catheter (26-gauge, Braun, Melsungen, Germany) was placed in the jugular vein to administer a volemic filling. The animal was kept in a plastic frame provided for this purpose for the acquisition of the images after checking the depth of the anesthesia, the animal was curarized to avoid respiratory movements (atracurium, 1.0 mg/kg by intrapitoneal injection).

Procedure of injurious-ventilation ARDS model

Injurious mechanical ventilation was induced by increasing the tidal volume to 20 ml/kg body weight, inhaled fraction of O_2 =1.0; maximum tracheal pressure = 40 cmH_2O, 0 PEEP, until a PaO_2/FIO_2 < 300 cmH_2O, and a respiratory rate of 30 bpm for 20 minutes. In control and bleomycin-injured rats on day 7 post-intratracheal instillation, LFOT was performed at baseline, followed by 4DCT image acquisition for 9 minutes. LFOT measurements were acquired prior to inducing VILI, followed by another set of LFOT measurements. Following this procedure, the animal was repositioned either higher or lower by adjusting the rotational stage remotely and a second set of imaging was obtained, so as to not image in the same location. At the end of this measurement the animals were euthanized by a barbiturate overdose (pentobarbital sodium at 220 mg/kg).

Lung fixation and histology

After euthanization, the entire lungs were excised from the rodent and inflated to physiological pressure and fixed at 20 cmH_2O and the trachea was tied with surgical string and submerged in 100% ethanol for preservation. The lungs were fixed in 4% paraformaldehyde at 20 cmH_2O and the left lungs were then excised for histological staining. 4 μm sections of the left lungs were dehydrated with a graded ethanol series and embedded in paraffin, prepared and stained with hematoxylin and eosin for qualitative histological evaluation.

Image Analysis

The dynamic CTs acquired and reconstructed following the strategy discussed in the previous section were used to study the dynamics of the lung parenchyma.

Several new challenges were discovered in this investigation; e.g. what mechanisms trigger pulmonary fibrosis in mechanically ventilated ARDS? How does alveolar strain contribute to or mitigate the systemic inflammatory response sense in drug-induced ARDS? What is the link between mechanical stresses induced to the lung tissue through atelectruma and the inflammatory response at an early stage of bleomycin-induced lung injury? How does the strain distribution (regional strain mechanics) vary across different regions of the lung in ARDS, and what factors influence this heterogeneity given the heterogeneous distribution of lung injury?

To address these points, the quantitative study of the cardiogenic motion of the lung parenchyma was conducted using elastic image registration to align images from different phases of the respiratory cycle. This registration process generated a displacement vector field representing local tissue movements. The divergence theorem was applied to compute the volume change. The Moving Least Squares (MLS) kernel-based convolution algorithm was used to compute the divergence, granting that linear relationships are well represented. This approach leverages principles related to the divergence theorem for understanding volumetric expansion or contraction within the lung tissue. The volume change is computed by multiplying the original volume by the divergence of the deformation field, while the strain was given by directly by the divergence.

These techniques relied on several python packages to perform computations, increase computation performance, parallelization and data storage for visual interpretation: Scikit provides various algorithms and is designed to work seamlessly with other Python numerical and scientific libraries (Van der Walt *et al.*, 2014). NumPy (Van Der Walt, Colbert and Varoquaux, 2011) provides a vast collection of mathematical functions to perform calculations on multi-dimensional arrays and matrices. VTK (visualization toolkit) was used for image processing,

image storage (Schroeder, Avila and Hoffman, 2000). Paraview was used to visualization, it is built upon VTK libraries (Ayachit, 2015).

Lung segmentation

Based on the image's histogram Otsu's algorithm was applied to initially find a lower luminosity bound that was used to partition the voxels as aerated and non-aerated (Otsu, 1979). An upper bound was manually determined by manual thresholding to carry out the segmentation. To classify the aerated voxels as proximal, intermediate and terminal, an iterative process was performed using a custom segmentation script developed in Python. The axial regions of the proximal bronchi were identified by carrying out a stepwise 3D erosion process. Assuming the proximal bronchi are quasi cylindrical, these bronchi were identified by linear regression and regions where volume will decrease linearly with respect to the number of erosion steps, based on the root mean square error. The primary bronchi were then recovered by morphological dilatation. Intermediate structures were subsequently identified as structures requiring less erosion steps than the primary bronchi. All the selected voxels which were not classified as proximal or intermediate were classified as terminal structures.

Image registration

Image registration plays a crucial role in quantifying regional changes in lung volume due to the complex nature of lung motion. Image registration is essential for accurately quantifying regional changes in lung volume by enabling comparison of images at different time points, facilitating the assessment of lung function and deformation. This study is a specific case, as in the previous study (Cercos-Pita *et al.*, 2022), this an extension of 4DCT lung tissue biomechanics to smaller length scales and higher temporal resolution than previously achieved, in live anesthetized rats under controlled ventilation.

Image registration (also known as image alignment) is the process of finding correspondences between two or more images, that is the transformation of mapping one image into the space of another, such that there is a high degree of affinity between the corresponding parts of the image and the differences between these two images is encoded in the transformation (Zitova and Flusser, 2003; Viergever *et al.*, 2016). The method applied in this study is colloquially known as intensity-based (area-based) where distances or similarities incorporating information from the entire images are used to find correspondences. In image registration, it is common to categorize methods with respect to the flexibility of the transformation model, e.g. rigid/affine or deformable (non-rigid). In which, specifically in this study, an elastic non-parametric deformation model based on diffeomorphic deformations was implemented. Initially proposed by Klein et al. (Klein *et al.*, 2011) and

published within the Python Imaging Registration Toolkit (PIRT) (https://pirt.readthedocs.io/index.html).

The demon's algorithm is an elastic, non-linear, non-parametric deformation model based upon diffeomorphic deformations which offers unique and useful properties. This is desirable in anatomical medical imaging to describe the transformations (now to be called deformations) between images. In an elastic deformation model, the term refers to the property of the deformations to be smooth, continuous, and able to stretch and bend without tearing or folding.

That is, topological integrity is maintained in the objects being deformed. In an "non-parametric" deformation model the modelling does not take into account any programmed assumptions about the mathematical form of the deformations, but instead, dynamically adjusts the deformations based on image intensity differences, allowing it to handle complex, data-driven deformations. Non-linear in the context of the Demons algorithm refers to the algorithm's ability to apply complex deformations that are not limited to simple translations, rotations and scaling. Instead, it can adjust to local variations in the image allowing for the detailed and intricate alignment of features between the moving and fixed images.

This property is imposed by a regularizing constraint and the cost function. To improve over previous methods (Leow *et al.*, 2007), a Lagranian regularizing constraint was incorporated. The cost function employed in our study is colloquially known as sum of squared differences (SSD). This similarity metric quantifies the alignment between two images. By calculating the cumulative square of intensity differences between corresponding pixels in the fixed and moving images. Lower SSD values indicated better alignment, as they imply smaller differences in pixel values between the images. This metric is particularly effective for registration tasks involving images of the same modality where intensity patterns are expected to be similar once the images are properly aligned.

The registration algorithm was applied in pairwise fashion. Pairwise registration was implemented with what is known as "backward" mapping, referring to aligning a moving image to a fixed image by inversely deforming the moving image. Instead of calculating the deformation needed to align the moving image directly to the fixed image, "forward" mapping, and "backward" mapping compute the transformation from the perspective of the fixed image, effectively asking, "how must the fixed image be deformed to match the moving image?" This approach offers computational advantages and improves the accuracy of the registration by focusing on the fixed image as the reference frame.

In PIRT, the specific registration method used is named "demons" after an analogy with Maxwell's Demons (Thirion, 1998). This method was previously tested against two other registration techniques prior to being selected (simpleElastix and PIRT "Gravity"), achieving an optimal minimization of registration errors. The results of these are not included in this report. This increases the image spatial resolution and

allows for computing the deformations field, the so-called strain field. The “demons” method previously mentioned, with diffeomorphic deformations properties implemented. Has offered the most robust method for this study.

Computation of volumetric changes

In the analysis of respiratory mechanics utilizing segmented voxels from CT scans, the divergence theorem was applied to accurately correlate movements within the respiratory system to volume changes and strain. By examining the displacement and deformation of voxel points throughout the respiratory cycle, volume change (Δv) was computed by equating the divergence of the deformation field to the voxel's surface area multiplied by the displacement distance. This computation facilitated the calculation of total volume change by multiplying the divergence by the original volume. Strain, indicating the degree of deformation, was directly derived from the divergence of the deformation field, providing insights into how regions of the lung expanded or contracted. To enhance the accuracy of these computations and address the limitations inherent in traditional Jacobian methods, a high-order Mean Least Squares (MLS) kernel-based convolution was employed. This approach involved a specialized kernel (W) for convolution and an MLS matrix (L) to correct for the truncation of the kernel's compact support, ensuring linear consistency and accuracy across the complex deformations observed during the respiratory cycle.

Results

Paper I. *Development of a robust and reproducible method for evaluation of absorbed doses in preclinical in-vivo μCT studies*

Study **I** introduced a feasible technique to quantify the radiation absorbed dose using solid state dosemeters for μCT imaging protocols. The dose measurements were benchmarked against the vendor-provided dose to evaluate how accurate they are. Further, the aim of the study was to evaluate absorbed doses in pre-clinical *in-vivo* μCT imaging to mitigate potential radiation-related effects on experimental outcomes. Absorbed dose measurements were done using both TLDs and OSLD with a PMMA phantom for various imaging protocols. A key objective was to demonstrate the novel use of NaCl-based OSLDs as a cost-effective, reliable, and simple method for dose assessments in μCT. Additionally, the study aimed to highlight potential discrepancies between the vendor-provided doses for these scan protocols and measured doses.

Table 5: Absorbed doses from the μCT for the default protocols. The data points represent the mean values of 6 measurements in mGy and standard deviation for LiF chips. The uncertainty refers to the average uncertainty of each measurement. Table from paper 1.

Vendor provided dose [mGy]		**FAST**	**NORMAL**	**ACCURATE**	**GATED**
		13	**299**	**420**	**673**
Position in phantom	1	22.8 ± 1.1	190 ± 8.7	225 ± 8.8	260 ± 11
	2	20.8 ± 1.6	176 ± 12	221 ± 12	231 ± 3.4
	3	19.9 ± 0.6	170 ± 8.9	212 ± 14	233 ± 5.8
	4	18.8 ± 1.8	161.8 ± 11	200 ± 24	207 ± 9.8

For the TLD, the dose decreased as expected from the surface to the centre of the phantom. The dose from the FAST protocol gave the lowest doses and the doses increased for the NORMAL, ACCURATE and GATED protocols in mentioned order. This is easily explained by the increase in number of projections as shown in Table 2. It was found for the FAST protocol that the measured doses were higher than the dose values provided by the system. In contrast, for the NORMAL,

ACCURATE and GATED protocols the measured doses were lower than the doses provided by the system for the respective protocols (Table 5).

Table 6: Absorbed doses from the μCT for the default protocols. The data points represent the mean values of 6 measurements in mGy and standard deviation for NaCl pellets. The uncertainty refers to the average uncertainty of each measurement. Table from paper 1.

Vendor provided dose [mGy]		**FAST**	**NORMAL**	**ACCURATE**	**GATED**
		13	**299**	**420**	**673**
Position in phantom	1	20.5 ± 3.7	173 ± 13	198 ± 4.8	224 ± 9.0
	2	18.8 ± 2.1	162 ± 3.0	181 ± 3.1	190 ± 10
	3	18.4 ± 4.0	149 ± 10	171 ± 4.3	185 ± 15
	4	18.0 ± 2.8	134 ± 12	161 ± 4.3	182 ± 11

Table 7: Percentage difference between system provided dose and the LiF chips (left) and NaCl pellets (right) response. Table from paper 1.

FAST	45%	38%
NORMAL	-46%	-55%
ACCURATE	-52%	-62%
GATED	-69%	-73%

The findings from Table 7 indicate that the low-dose fast scan under-estimates the dose while all other scans over-estimate the dose.

Paper II. *In-vivo synchrotron phase-contrast imaging of Lung Tissue Biomechanics in a Rat Model of Ventilator and Bleomycin-Induced Injury*

In this study, we used four-dimensional synchrotron phase contrast micro-computed tomography (μCT) to dynamically observe local lung tissue strain (ε) in mechanically ventilated rats with both healthy and damaged lungs due to extracellular matrix changes, caused 7 days after bleomycin intratracheal instillation in combination with high tidal volume ventilation. The main findings indicated: 1) local strain (ϵ) decreased in aerated acini after bleomycin injury (figure 9); 2) this decrease in local ϵ correlated with an increase in dynamic stiffness (H) and energy dissipation, as indicated by the damping coefficient (G) (figure 10); 3) tissue hysteresivity (η) was notably lowered by early injury from bleomycin and ventilation with high tidal volume (VT) (figure 11); 4) a significant negative relationship was observed between global respiratory elastance (H) and local strain when subjected to the stress of positive pressure ventilation (figure 12).

Of the respiratory parameters, only driving pressure (ΔP) was significantly higher after injurious ventilation in controls. During injurious ventilation, the peak inspiratory pressure corresponded to a Pmax of~41 cmH_2O corresponding to a tidal volume of~65 ml/kg.

Table 8. Respiratory parameters. Fmax: peak inspiratory flow, Pmax: peak inspiratory pressure; PEEP: positive end-expiratory pressure; driving pressure ΔP: Pmax – PEEP; VT: tidal volume at baseline and during imaging; RR: respiratory rate. BL: baseline; VILI: injurious ventilation. *: p<0.05 vs. Control BL. Table from paper 2.

		Pmax	**PEEP**	**ΔP**	**RR**	**VT**
		cmH2O	**cmH2O**	**cmH2O**	**bpm**	**ml**
Control BL		10.5±1.2	5.1±0.5	5.3±0.8	74.9±14.4	5.7±1.5
Control VILI		13.8±7.1	5.2±0.7	8.6±7.7*	81.9±8.3	5.6±1.2
Bleo BL		12±2.8	4.7±0.7	7.3±2.6	85.1±6.7	5.9±2.0
Bleo VILI		11±1.9	4.6±0.5	6.4±2	83±12.8	5.1±0.6

This is further corroborated by the significant reduction in parenchymal strain observed in the bleomycin-treated animals, supporting the evidence of lung stiffness and decreased compliance. The respiratory mechanical parameters in these animals showed a significant increase in tissue elastance (H) and damping (G), pointing to increased lung stiffness and resistance to deformation. However, the unchanged airway resistance (Raw) and hysterisivity (η) highlight that the observed alterations are specific to lung tissue properties, indicating a targeted impact of bleomycin on lung tissue rather than a generalized effect on airway dynamics (figure 11).

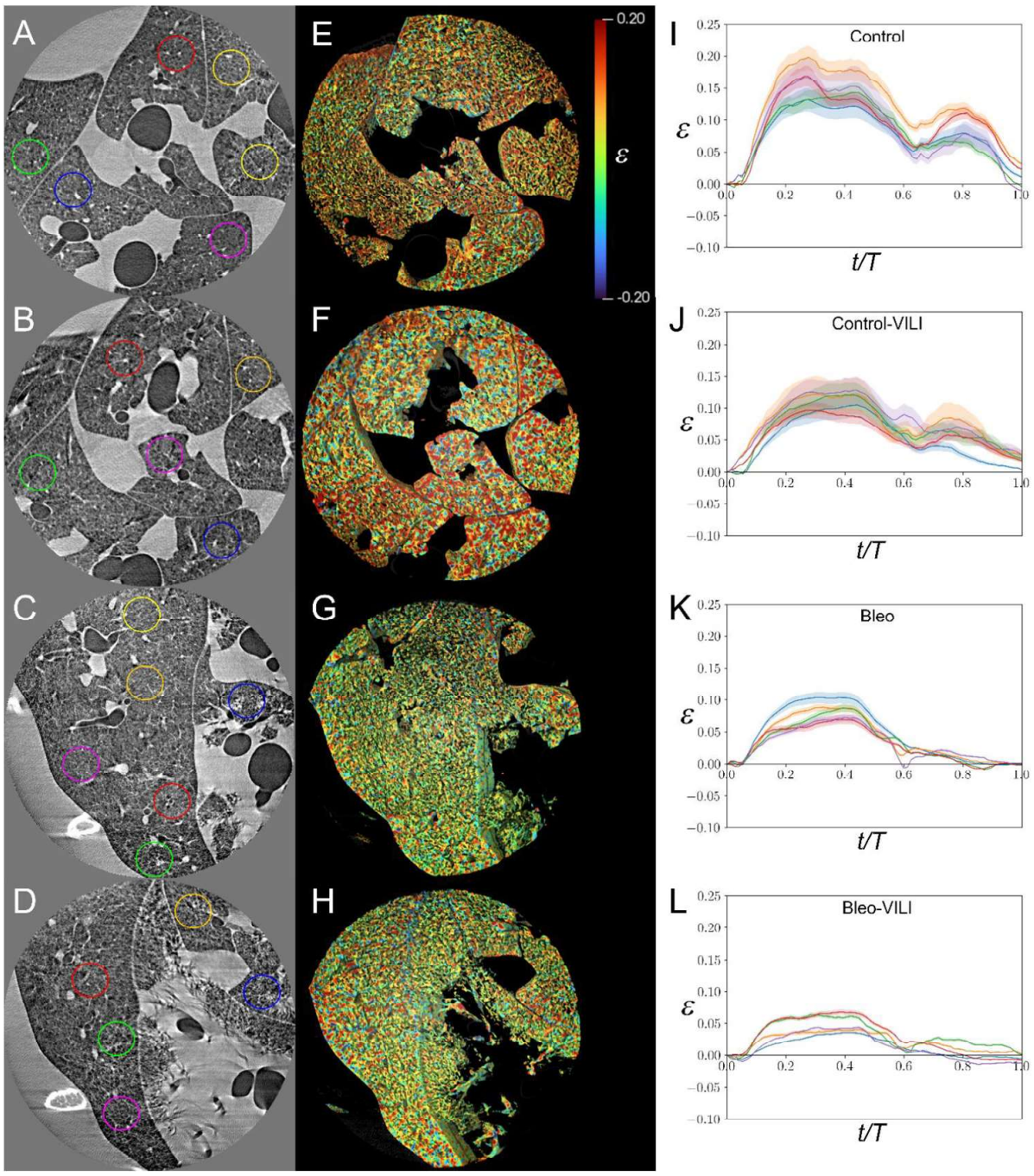

Figure 9. A-D: representative phase-contrast CT images in a Control (A), high-VT ventilation (B), Bleomycin-injured (C) and Bleomycin after high-VT ventilation (D) rat; E-H: corresponding strain (ε) maps; I-L: corresponding dynamic ε curves as a function time relative to the beginning of the respiratory cycle (t/T), within ROI's of same color as in A-D. Note the reduced tissue strain and slope in bleomycin-injured lung and further reduction after high-VT ventilation. Figure from paper 2.

It is witnessed in the representative scans of the different groups. The average strain peaks normalized to the end-expiratory volume show maps of local microscopic tissue ε vs. time within all six ROI's in the strain map. In animals instilled with bleomycin, there was a noticeable reduction in maximal tissue strain

at end-inspiration, indicating impaired lung expandability or increased stiffness, a likely consequence of bleomycin-induced lung injury (figure 10).

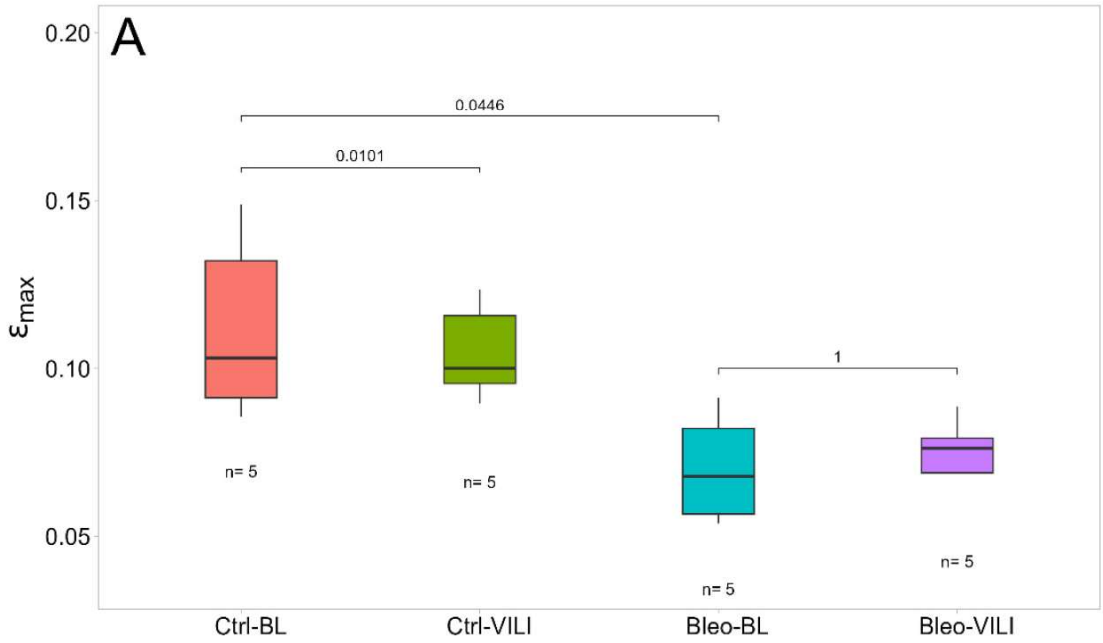

Figure 10. A: maximal local inspiratory lung parenchymal strain (ϵ) BL: baseline; VILI: injurious ventilation. P-values are presented by a generalized linear regression model. Figure from paper 2.

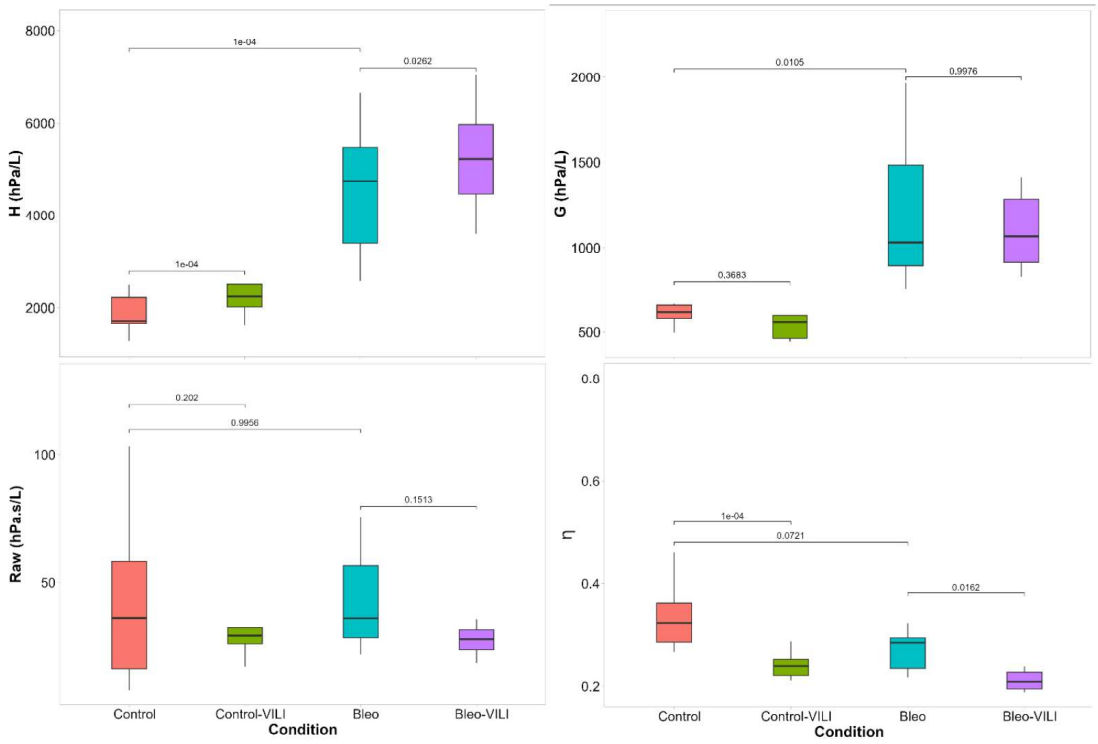

Figure 11. Oscillatory respiratory mechanical parameters. H: respiratory tissue elastance; G: tissue damping; Raw: airway resistance; η: hysterisivity. P-values are presented by a generalized linear regression model. Figure from paper 2.

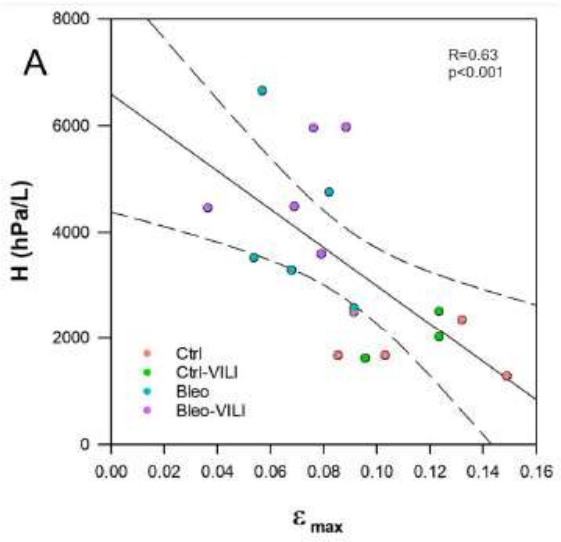

Figure 12. Relationship between respiratory tissue elastance (H) and maximal local parenchymal strain (ϵ_{max}). Ctrl: Control; Ctrl-VILI: Control after high-tidal volume ventilation; Bleo: bleomycin-induced lung injury; Bleo-VILI: bleomycin after high-tidal volume ventilation. Figure from paper 2.

The regression analysis of elastance and parenchymal strain shown a significant inverse relationship indicating that as lung tissue became stiffer (higher respiratory elastance), the ability of the lung tissue to expand (parenchymal strain) decreased.

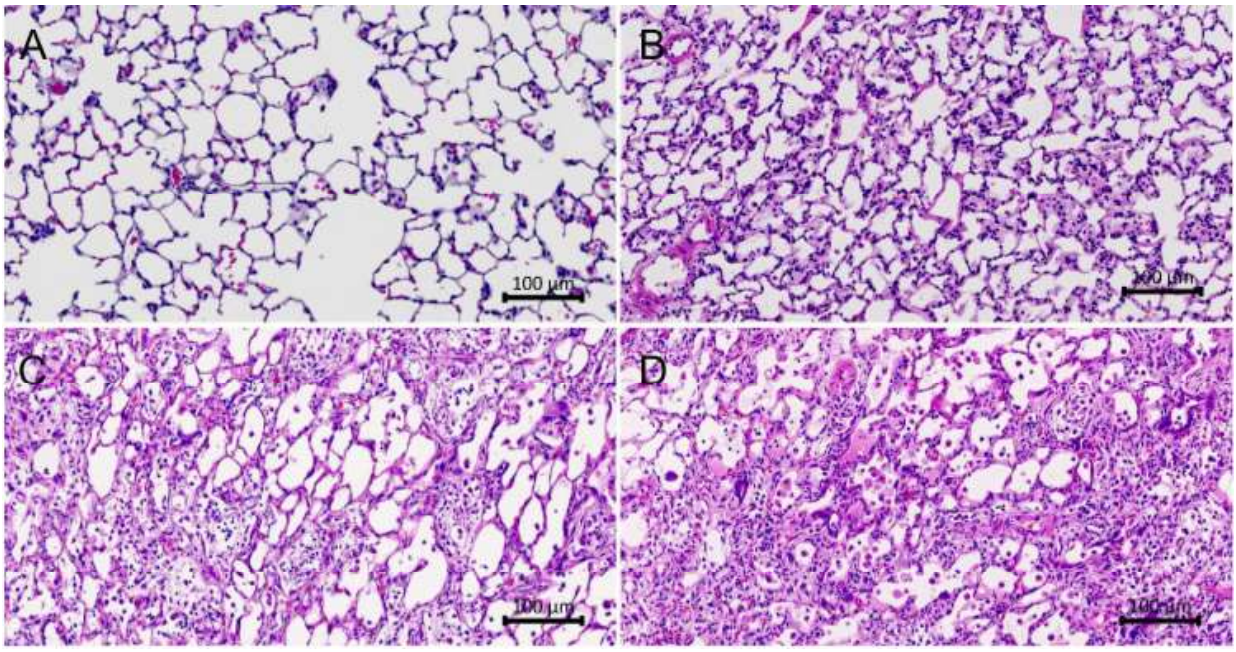

Figure 13. Light microscopic images of the lung tissue. Representative hematoxylin & Eosin stains in; A: control lung; B: control after 20 minutes of injurious mechanical ventilation within abnormal appearing regions. Signs of injury include: neutrophilic cellular infiltration (dark blue dots), alveolar wall thickening and occasional hyaline membranes (extra pink tissue); C: day 7 post bleomycin intratracheal instillation with gross inflammation and alteration in the alveolar architecture and interstitial matrix thickening with significant increase in concentration of hyaline membranes with clear diffuse alveolar damage; D: bleomycin injured lung with additional 20 minutes of injurious mechanical ventilation with somewhat greater inflammation and few alveolar hyaline membranes. Figure from paper 2.

Before the application of injurious ventilation, control animals showed no signs of lung tissue damage, indicating that their lungs were in a normal or unaffected baseline condition due to the experimental setup (figure 13). However, after injurious ventilation, these controls exhibited mild leukocyte margination, extracellular matrix deposition, and occasional thickening of alveolar septa, suggesting the early stages of lung injury. This inflammatory response and the beginnings of fibrotic changes, such as the deposition of extracellular matrix and alveolar septa thickening, can impair gas exchange and lung compliance. Despite these signs of injury, there were interspersed regions within the lung that appeared normal, without significant hyaline membrane formation or edema, indicating that the injury was not uniformly severe and did not reach the levels often associated with ARDS or severe acute lung injury. As the hallmark of diffuse alveolar damage is the presence of hyaline membrane formation. In contrast, animals instilled with bleomycin exhibited more severe symptoms, including extensive matrix deposition, thickening of alveolar walls, intra-alveolar edema, neutrophilic infiltrates, and widespread micro-atelectasis in all regions examined by histological sectioning. These findings are characteristic of severe lung injury and fibrosis, highlighting the significant impact of bleomycin on inducing inflammation, fibrotic changes, and impaired lung function with reduced gas exchange capability.

Discussion

Paper I

The implications this study has for preclinical research has several impactful outcomes.

The differences observed in the measured doses using TLDs and OSLDs may partly be explained by the different effective atomic numbers of the LiF and NaCl, that results in different energy dependence. Correction factors for this effect have been suggested by Waldner et. al. (Waldner and Bernhardsson, 2018). The x-ray spectrum adds complexity since a calibration factor for representing an average energy. Here, the effective mean energy of the X-ray spectrum was based upon SpekCalc. This may be accurate to do for the low-dose "FAST" scan and hence why the results are similar. However, this may be less accurate as the dose increases. For future studies, one way to further this would be to vary the number of projections, while keeping all other parameters the same.

The agreement between the two independent dosemeters suggests a consistency in their capabilities. This consistency strengthens the argument that the discrepancy observed between the vendor-provided dose indicates that the method or data used by the vendor may need reassessment. It's possible that the vendor's methods for estimate the radiation absorbed dose is significantly different from the methods we used.

The FAST scan protocol's dose was 39% higher than the vendor-provided values, while the NORMAL, ACCURATE, and GATED protocols indicated lower doses by 36% to 57%, respectively, which reveals a notable discrepancy in vendor-reported and measured dose values. This discrepancy highlights the necessity for validation of vendor-provided dose estimations with empirical measurements. The fact that for most protocols, the system underestimates the dose is reassuring from an animal safety perspective, indicating that using vendor-provided values would not result in overexposure. However, this discrepancy also suggests that researchers might inadvertently use less exposure than necessary resulting in sub-optimal imaging quality.

Another observation is the lack of similar studies in the literature. Though, there are other works that have utilized LiF as a dosemeter in similar studies, none have specifically used the MCP-N chip which is hailed for its sensitivity. No, other

studies have used NaCl pellets, although some have used OSLDs. Furthermore, no studies have been carried out specifically on the MILabs xUHR-μCT scanner. The studies that do report using the same voltage setting, other parameters such as tube filtration are different. Thus, it is not possible to perform a one-to-one comparsion to the literature. An interesting task would be to perform an inter-institutional comparisons using the PMMA phantom and NaCl pellets, for example (Mannheim *et al.*, 2019; McDougald *et al.*, 2020; Gadelha *et al.*, 2020) to address this issue.

The findings stress the need for standardized, easily repeatable dose measurement methods for μCT scanners, akin to those established for clinical scanners. Without such standards, ensuring consistent and accurate dosimetry across different studies and scanners becomes challenging, potentially affecting the reproducibility and comparability of research findings. The validation of NaCl pellets as a cost-effective, easily accessible dosemeter material for preclinical setups is a significant outcome. It provides researchers with more options for accurate dosimetry, especially in resource-limited settings, and promotes the broader adoption of rigorous dose measurement practices.

A limitation of this study is that it only considers at the default imaging protocols of the μCT system. Future studies may apply the same technique to investigate custom *in-vivo* imaging protocols using phantoms that include other image quality parameters such as contrast materials to calculate the SNR and CNR. One could assess the inverse-square dose-to-noise relationship in a single scan.

Paper II

Despite significant improvements in protective mechanical ventilation strategies to treat patients with ARDS, overall mortality remains high (Network, 2000). Significant gaps remain in the understanding of how mechanical ventilation ventilates and injures the lungs (Slutsky and Ranieri, 2013; Henderson *et al.*, 2017) and how local strain is related to structural and functional (e.g. inflammatory, mechanotransductory) changes in the ECM.

The physical and molecular basis remains unknown for the reduction in strain in the aerated acini of the bleomycin diseased lungs. A disturbance in the ECM is a likely culprit. There are numerous theories to the reason of heightened lung stiffness due to alterations in the ECM components (Burgess and Harmsen, 2022). Future studies should focus on examining the excised lung tissue samples from our study by using advanced imaging techniques that have recently been applied to study different aspects of lung disease. Recently atomic force microscopy (AFM) has been used to assess the ECM after bleomycin-injury (Júnior *et al.*, 2023). One finding suggests that during the inflammatory phase of bleomycin-injury conformation of the fibres in the ECM alters, resulting in stiffening of the ECM. Another technique to image collagen fibres in a different mouse models instilled with bleomycin-injury utilized

a technique called harmonic generation microscopy (SHG) (Dobrinskikh *et al.*, 2021), to distinguish genes and transcripts that may influence lung fibrosis. Another fascinating technique recently applied is known as fourier transform infrared spectroscopy (FTIR) which was utilized to elucidate biochemical alterations with improvements over classical hemotoxycin and trichrome staining in sections of lungs post-bleomycin induced lung injury (Suryadevara *et al.*, 2020). These methods aim to visualize both structural and biochemical changes in the ECM of the lung parenchyma and may improve our understanding of the pathophysiological mechanisms underlying lung injury.

CT is a powerful imaging tool for investigating the dynamics of ARDS and VILI. Currently longitudinal studies to investigate alveolar dynamic changes may be too costly or not feasible for synchrotron imaging or not possible with commercially-available μCT systems. Recent attempts have made significant progress with laboratory imaging systems using liquid-metal jet technology (Excillium AB, Kista, Sweden). Acquiring *in-vivo* images with spatial scales down to 30-60 μm (Murrie *et al.*, 2020; Shaker *et al.*, 2021). Though these were not dynamic studies nor the spatial resolution was sufficient to obtain images at the alveolar scale. Synchrotrons with their unique capabilities to perform propagation based phase-contrast imaging and their extremely high flux offer the only technique to resolve lungs with sufficient contrast to visualize the dynamics of the alveolar acinus (Cercos-Pita *et al.*, 2022). A notable limitation of our study is the insufficient spatial resolution and the inadequacy in correction of motion blur, which precludes the visualization of individual alveoli under dynamic conditions. This would require shorter image acquisition times with higher flux than possible at ID-17 beamline at ESRF. Along with smaller pixel sizes than the detector used in our study. Implementing these requirements at a 4^{th} generation synchrotron facility would be a logical next improvement. Yet, such a beamline does not yet exist.

Conclusions

In Study **I**, Significant contributions to the ongoing dialogue about the accuracy of dose measurements in preclinical imaging and the implications for research validity and animal welfare was done. By highlighting the discrepancies in measured vs vendor provided doses and the need for standardization, it paves the way for improvements in dosimetry practices in the field of preclinical research. Further research, focusing on overcoming the study's limitations and exploring new methodologies for dose measurement, will be essential in advancing our understanding and application of safe, accurate imaging protocols.

Radiation absorbed dose for longitudinal dynamic CT imaging is the largest hurdle to overcome for translation of this technology to the clinic. It remains an essential research tool for investigating the effect of the ventilator and lung injury models on lung structure and function in animal models. Study I in this work significantly contributes to the ongoing dialogue about the accuracy of dose measurements in preclinical imaging and the implications for research validity and animal welfare. By highlighting the discrepancies in dose estimations and the need for standardization, it improves dosimetry practices in the field of preclinical research. Further research by applying this technique to other imaging modalities will be essential in advancing our understanding and application of safe, accurate imaging protocols.

In Study **II**, evidence supporting the initial hypothesis that on the microscopic level, the tidal ventilation induces changes in the parenchyma that cause inhomogeneous stress in the acinar compartments was found. The dynamic imaging of local microscopic tissue strain (ε) in intact, closed-chest rats via 4D synchrotron phase contrast microcomputed tomography (μCT) elucidates regional viscoelastic properties of the aveolar acinus. Seven days post-bleomycin administration, a diminution in ε within aerated acini is observable. High tidal volume (VT) ventilation exacerbates this effect, leading to an increase in dynamic respiratory elastance and a further reduction in ε in unaffected lung tissue. Both bleomycin-induced lung injury and high VT ventilation contribute to a decrease in respiratory tissue hysterisitivity (η), indicating a diminished capacity for energy dissipation relative to storage within the lung. Ongoing research aims to identify the specific structural changes occurring within lung parenchymal tissue components at this early stage of VILI (Sgalla *et al.*, 2018).

This research emphasizes the critical need for ventilation strategies that are sensitive to the underlying pathophysiological changes in lung tissue mechanics, particularly in the context of lung injury. The insights into the biological mechanisms driving these changes, including alterations in the ECM and surfactant dysfunction, provide valuable targets for therapeutic intervention. Future studies focusing on elucidating the detailed molecular pathways involved in these processes, and how they interact with mechanical forces during ventilation, will be crucial. Additionally, there's a need for exploring how these findings translate to clinical practice, including the development of personalized ventilation strategies that can adapt to the evolving mechanical and biological landscape of the injured lung. Overall, this study lays a foundation for a more nuanced understanding of lung injury and mechanical ventilation, pointing the way toward more effective and less injurious respiratory support for patients with acute lung injury or chronic lung diseases.

There is currently no known ventilation strategy to completely avoid injury to the lungs. ARDS and VILI is multifaceted, and requires an interdisciplinary approach to improve our understanding of the controversies about ventilation strategy. This work demonstrates that dynamic imaging of lung deformation at the acinar scale and interpretation of the data on regional lung function is critical to advancing our understanding of the effect to regional alveolar mechanics.

References

Albers J, Wagner W L, Fiedler M O, Rothermel A, Wünnemann F, Di Lillo F, Dreossi D, Sodini N, Baratella E and Confalonieri M 2023 High resolution propagation-based lung imaging at clinically relevant X-ray dose levels *Scientific Reports* **13** 4788

Ayachit U 2015 *The paraview guide: a parallel visualization application*: Kitware, Inc.)

B. Moore B, Lawson W E, Oury T D, Sisson T H, Raghavendran K and Hogaboam C M 2013 Animal models of fibrotic lung disease *American journal of respiratory cell and molecular biology* **49** 167-79

Bates J H and Smith B J 2018 Ventilator-induced lung injury and lung mechanics *Annals of translational medicine* **6**

Bellani G, Laffey J G, Pham T, Fan E, Brochard L, Esteban A, Gattinoni L, Van Haren F, Larsson A and McAuley D F 2016a Epidemiology, patterns of care, and mortality for patients with acute respiratory distress syndrome in intensive care units in 50 countries *Jama* **315** 788-800

Bellani G, Laffey J G, Pham T, Fan E, Investigators L S and Group t E T 2016b The LUNG SAFE study: a presentation of the prevalence of ARDS according to the Berlin Definition! *Critical care* **20** 1-2

Berghen N, Dekoster K, Marien E, Dabin J, Hillen A, Wouters J, Deferme J, Vosselman T, Tiest E and Lox M 2019 Radiosafe micro-computed tomography for longitudinal evaluation of murine disease models *Scientific reports* **9** 17598

Bernhardsson C, Christiansson M, Mattsson S and Rääf C L 2009 Household salt as a retrospective dosemeter using optically stimulated luminescence *Radiation and environmental biophysics* **48** 21-8

Bernhardsson C, Waldner L and Vodovatov A 2017 Advancements in prospective dosimetry with NaCl read-out by optically stimulated luminescence

Best A C, Meng J, Lynch A M, Bozic C M, Miller D, Grunwald G K and Lynch D A 2008 Idiopathic pulmonary fibrosis: physiologic tests, quantitative CT indexes, and CT visual scores as predictors of mortality *Radiology* **246** 935-40

Bräuer-Krisch E, Requardt H, Regnard P, Corde S, Siegbahn E, LeDuc G, Brochard T, Blattmann H, Laissue J and Bravin A 2005 New irradiation geometry for microbeam radiation therapy *Physics in Medicine & Biology* **50** 3103

Bretin F, Bahri M A, Luxen A, Phillips C, Plenevaux A and Seret A 2015 Monte Carlo simulations of the dose from imaging with GE eXplore 120 micro-CT using gate *Medical Physics* **42** 5711-9

Broche L, Perchiazzi G, Porra L, Tannoia A, Pellegrini M, Derosa S, Sindaco A, Borges J B, Degrugilliers L and Larsson A 2017 Dynamic mechanical interactions between neighboring airspaces determine cyclic opening and closure in injured lung *Critical care medicine* **45** 687-94

Burgess J K and Harmsen M C 2022 Chronic lung diseases: entangled in extracellular matrix *European Respiratory Review* **31**
Carlson S K, Classic K L, Bender C E and Russell S J 2007 Small animal absorbed radiation dose from serial micro-computed tomography imaging *Molecular Imaging and Biology* **9** 78-82
Cercos-Pita J-L, Fardin L, Leclerc H, Maury B, Perchiazzi G, Bravin A and Bayat S 2022 Lung tissue biomechanics imaged with synchrotron phase contrast microtomography in live rats *Scientific Reports* **12** 5056
Clark D P and Badea C 2014 Micro-CT of rodents: state-of-the-art and future perspectives *Physica medica* **30** 619-34
Cozzi D, Cavigli E, Moroni C, Smorchkova O, Zantonelli G, Pradella S and Miele V 2021 Ground-glass opacity (GGO): a review of the differential diagnosis in the era of COVID-19 *Japanese journal of radiology* **39** 721-32
Deak P and Kalender W *World Congress on Medical Physics and Biomedical Engineering, September 7-12, 2009, Munich, Germany: Vol. 25/2 Diagnostic Imaging,2009),* vol. Series*)*: Springer) pp 338-41
Detombe S A, Dunmore-Buyze J, Petrov I E and Drangova M 2013 X-ray dose delivered during a longitudinal micro-CT study has no adverse effect on cardiac and pulmonary tissue in C57BL/6 mice *Acta radiologica* **54** 435-41
Dixon R L, Anderson J A and Bakalyar D M 2010 Comprehensive methodology for the evaluation of radiation dose in x-ray computed tomography
Dobrinskikh E, Estrella A M, Hennessy C E, Hara N, Schwarz M I, Kurche J S, Yang I V and Schwartz D A 2021 Genes, other than Muc5b, play a role in bleomycin-induced lung fibrosis *American Journal of Physiology-Lung Cellular and Molecular Physiology* **321** L440-L50
Drangova M, Ford N L, Detombe S A, Wheatley A R and Holdsworth D W 2007 Fast retrospectively gated quantitative four-dimensional (4D) cardiac micro computed tomography imaging of free-breathing mice *Investigative radiology* **42** 85-94
Dubsky S, Hooper S B, Siu K K and Fouras A 2012 Synchrotron-based dynamic computed tomography of tissue motion for regional lung function measurement *Journal of The Royal Society Interface* **9** 2213-24
Ekendahl D, Bulánek B and Judas L 2016 A low-cost personal dosemeter based on optically stimulated luminescence (OSL) of common household salt (NaCl) *Radiation Measurements* **85** 93-8
Elleaume H, Charvet A, Berkvens P, Berruyer G, Brochard T, Dabin Y, Dominguez M, Draperi A, Fiedler S and Goujon G 1999 Instrumentation of the ESRF medical imaging facility *Nuclear Instruments and Methods in Physics Research Section A: Accelerators, Spectrometers, Detectors and Associated Equipment* **428** 513-27
Fardin L 2019 In-vivo dynamic 3D phase-contrast microscopy: a novel tool to investigate the mechanisms of ventilator induced lung injury. Université Grenoble Alpes)
Fardin L, Broche L, Lovric G, Mittone A, Stephanov O, Larsson A, Bravin A and Bayat S 2021 Imaging atelectrauma in ventilator-induced lung injury using 4D X-ray microscopy *Scientific Reports* **11** 4236
Figueroa S D, Winkelmann C T, Miller W H, Volkert W A and Hoffman T J 2008 TLD assessment of mouse dosimetry during microCT imaging *Medical physics* **35** 3866-74
Fitzgerald R 2000 Phase-sensitive x-ray imaging *Physics today* **53** 23-6

Ford E C, Mageras G, Yorke E and Ling C 2003 Respiration-correlated spiral CT: a method of measuring respiratory-induced anatomic motion for radiation treatment planning *Medical physics* **30** 88-97
Ford N, Thornton M and Holdsworth D 2003 Fundamental image quality limits for microcomputed tomography in small animals *Medical physics* **30** 2869-77
Ford N L, Nikolov H N, Norley C J, Thornton M M, Foster P J, Drangova M and Holdsworth D W 2005 Prospective respiratory-gated micro-CT of free breathing rodents *Medical physics* **32** 2888-98
Gadelha R M, Ferreira A V, Souza G A C, Silva J B and Mamede M 2020 Image quality evaluation for two different positron emitters in a preclinical PET scanner *Brazilian Journal of Radiation Sciences* **8**
Gattinoni L, Caironi P, Pelosi P and Goodman L R 2001 What has computed tomography taught us about the acute respiratory distress syndrome? *American journal of respiratory and critical care medicine* **164** 1701-11
Giuranno L, Ient J, De Ruysscher D and Vooijs M A 2019 Radiation-induced lung injury (RILI) *Frontiers in oncology* **9** 877
Hansen V, Murray A, Buylaert J-P, Yeo E-Y and Thomsen K 2015 A new irradiated quartz for beta source calibration *Radiation Measurements* **81** 123-7
Henderson W R, Chen L, Amato M B and Brochard L J 2017 Fifty years of research in ARDS. Respiratory mechanics in acute respiratory distress syndrome *American journal of respiratory and critical care medicine* **196** 822-33
Hernandez L A, Peevy K J, Moise A A and Parker J C 1989 Chest wall restriction limits high airway pressure-induced lung injury in young rabbits *Journal of Applied Physiology* **66** 2364-8
Hubmayr R D and Kallet R H 2018 Understanding pulmonary stress-strain relationships in severe ARDS and its implications for designing a safer approach to setting the ventilator *Respiratory care* **63** 219-26
Humphries S M, Mackintosh J A, Jo H E, Walsh S L, Silva M, Calandriello L, Chapman S, Ellis S, Glaspole I and Goh N 2022 Quantitative computed tomography predicts outcomes in idiopathic pulmonary fibrosis *Respirology* **27** 1045-53
Hupfer M, Kolditz D, Nowak T, Eisa F, Brauweiler R and Kalender W A 2012 Dosimetry concepts for scanner quality assurance and tissue dose assessment in micro-CT *Medical physics* **39** 658-70
Jacob R E, Carson J P, Thomas M and Einstein D R 2013 Dynamic multiscale boundary conditions for 4D CT of healthy and emphysematous rats *PloS one* **8** e65874
Júnior C, Ulldemolins A, Narciso M, Almendros I, Farré R, Navajas D, López J, Eroles M, Rico F and Gavara N 2023 Multi-step extracellular matrix remodelling and stiffening in the development of idiopathic pulmonary fibrosis *International Journal of Molecular Sciences* **24** 1708
Klein A, Kroon D-J, Hoogeveen Y, Kool L J S, Renema W K J and Slump C H *Medical Imaging 2011: Image Processing,2011),* vol. Series 7962*)*: SPIE) pp 632-9
Knudsen L, Lopez-Rodriguez E, Berndt L, Steffen L, Ruppert C, Bates J H, Ochs M and Smith B J 2018 Alveolar micromechanics in bleomycin-induced lung injury *American journal of respiratory cell and molecular biology* **59** 757-69
Krestel E 1990 Imaging systems for medical diagnostics
Kunihiro Y, Matsumoto T, Murakami T, Shimokawa M, Kamei H, Tanaka N and Ito K 2023 A quantitative analysis of long-term follow-up computed tomography of

idiopathic pulmonary fibrosis: the correlation with the progression and prognosis *Acta Radiologica* 02841851231175252
Leow A D, Yanovsky I, Chiang M-C, Lee A D, Klunder A D, Lu A, Becker J T, Davis S W, Toga A W and Thompson P M 2007 Statistical properties of Jacobian maps and the realization of unbiased large-deformation nonlinear image registration *IEEE transactions on medical imaging* **26** 822-32
Li X, Zhang D and Liu B 2013 Monte Carlo assessment of CT dose equilibration in PMMA and water cylinders with diameters from 6 to 55 cm *Medical Physics* **40** 031903
Liu T, De Los Santos F G and Phan S H 2017 The bleomycin model of pulmonary fibrosis *Fibrosis: Methods and Protocols* 27-42
Lovric G, Broche L, Schleputz C, Fardin L, Schittny J, Larsson A S and Bayat S 2018 *D105. CRITICAL CARE: VENTILATOR INDUCED LUNG INJURY AND ARDS-FROM MICE TO BIOMARKERS IN ARDS*: American Thoracic Society) pp A7526-A
Lovric G, Mokso R, Arcadu F, Vogiatzis Oikonomidis I, Schittny J C, Roth-Kleiner M and Stampanoni M 2017 Tomographic in vivo microscopy for the study of lung physiology at the alveolar level *Scientific reports* **7** 12545
Low D A, Nystrom M, Kalinin E, Parikh P, Dempsey J F, Bradley J D, Mutic S, Wahab S H, Islam T and Christensen G 2003 A method for the reconstruction of four-dimensional synchronized CT scans acquired during free breathing *Medical physics* **30** 1254-63
Mannheim J G, Mamach M, Reder S, Traxl A, Mucha N, Disselhorst J A, Mittelhäuser M, Kuntner C, Thackeray J T and Ziegler S 2019 Reproducibility and comparability of preclinical PET imaging data: a multicenter small-animal PET study *Journal of Nuclear Medicine* **60** 1483-91
Matute-Bello G, Frevert C W and Martin T R 2008 Animal models of acute lung injury *American Journal of Physiology-Lung Cellular and Molecular Physiology* **295** L379-L99
McDougald W, Vanhove C, Lehnert A, Lewellen B, Wright J, Mingarelli M, Corral C A, Schneider J E, Plein S and Newby D E 2020 Standardization of preclinical PET/CT imaging to improve quantitative accuracy, precision, and reproducibility: a multicenter study *Journal of Nuclear Medicine* **61** 461-8
Meganck J A and Liu B 2017 Dosimetry in micro-computed tomography: a review of the measurement methods, impacts, and characterization of the quantum GX imaging system *Molecular Imaging and Biology* **19** 499-511
Mendez C, Colpo N, Duzenli C, Atwal P and Gill B 2018 Development of a phantom for dosimetric comparison of murine micro-CT protocols with optically stimulated luminescent dosimeters *Medical Physics* **45** 3974-9
Mittone A, Manakov I, Broche L, Jarnias C, Coan P and Bravin A 2017 Characterization of a sCMOS-based high-resolution imaging system *Journal of synchrotron radiation* **24** 1226-36
Mokso R, Schwyn D A, Walker S M, Doube M, Wicklein M, Müller T, Stampanoni M, Taylor G K and Krapp H G 2015 Four-dimensional in vivo X-ray microscopy with projection-guided gating *Scientific Reports* **5** 8727
Momose A, Takeda T, Itai Y and Hirano K 1996 Phase–contrast X–ray computed tomography for observing biological soft tissues *Nature medicine* **2** 473-5

Murrie R P, Werdiger F, Donnelley M, Lin Y-w, Carnibella R P, Samarage C R, Pinar I, Preissner M, Wang J and Li J 2020 Real-time in vivo imaging of regional lung function in a mouse model of cystic fibrosis on a laboratory X-ray source *Scientific reports* **10** 447

Muscedere J, Mullen J, Gan K and Slutsky A 1994 Tidal ventilation at low airway pressures can augment lung injury *American journal of respiratory and critical care medicine* **149** 1327-34

Namati E, Chon D, Thiesse J, Hoffman E, De Ryk J, Ross A and McLennan G 2006 In vivo micro-CT lung imaging via a computer-controlled intermittent iso-pressure breath hold (IIBH) technique *Physics in medicine & biology* **51** 6061

Network A R D S 2000 Ventilation with lower tidal volumes as compared with traditional tidal volumes for acute lung injury and the acute respiratory distress syndrome *New England Journal of Medicine* **342** 1301-8

Nieman G, Kollisch-Singule M, Ramcharran H, Satalin J, Blair S, Gatto L A, Andrews P, Ghosh A, Kaczka D W and Gaver D 2022 Unshrinking the baby lung to calm the VILI vortex *Critical Care* **26** 1-14

Nieman G F, Kaczka D W, Andrews P L, Ghosh A, Al-Khalisy H, Camporota L, Satalin J, Herrmann J and Habashi N M 2023 First stabilize and then gradually recruit: a paradigm shift in protective mechanical ventilation for acute lung injury *Journal of clinical medicine* **12** 4633

Otsu N 1979 A threshold selection method from gray-level histograms *IEEE transactions on systems, man, and cybernetics* **9** 62-6

Perchiazzi G, Rylander C, Derosa S, Pellegrini M, Pitagora L, Polieri D, Vena A, Tannoia A, Fiore T and Hedenstierna G 2014 Regional distribution of lung compliance by image analysis of computed tomograms *Respiratory physiology & neurobiology* **201** 60-70

Poludniowski G, Landry G, Deblois F, Evans P and Verhaegen F 2009 SpekCalc: a program to calculate photon spectra from tungsten anode x-ray tubes *Physics in Medicine & Biology* **54** N433

Porra L, Broche L, Degrugilliers L, Albu G, Malaspinas I, Doras C, Wallin M, Hallbäck M, Habre W and Bayat S 2017 Synchrotron imaging shows effect of ventilator settings on intrabreath cyclic changes in pulmonary blood volume *American journal of respiratory cell and molecular biology* **57** 459-67

Porra L, Monfraix S, Berruyer G, Le Duc G, Nemoz C, Thomlinson W, Suortti P, Sovijarvi A and Bayat S 2004 Effect of tidal volume on distribution of ventilation assessed by synchrotron radiation CT in rabbit *Journal of Applied Physiology* **96** 1899-908

Preissner M, Murrie R, Pinar I, Werdiger F, Carnibella R, Zosky G, Fouras A and Dubsky S 2018 High resolution propagation-based imaging system for in vivo dynamic computed tomography of lungs in small animals *Physics in Medicine & Biology* **63** 08NT3

Ranieri V, Rubenfeld G, Thompson B, Ferguson N, Caldwell E, Fan E and Camporota L 2012 Acute respiratory distress syndrome: the Berlin Definition *Jama* **307** 2526-33

Russotto V, Bellani G and Foti G 2018 Respiratory mechanics in patients with acute respiratory distress syndrome *Annals of translational medicine* **6**

Schroeder W J, Avila L S and Hoffman W 2000 Visualizing with VTK: a tutorial *IEEE Computer graphics and applications* **20** 20-7
Sera T, Yokota H, Tanaka G, Uesugi K, Yagi N and Schroter R C 2013 Murine pulmonary acinar mechanics during quasi-static inflation using synchrotron refraction-enhanced computed tomography *Journal of Applied Physiology* **115** 219-28
Sgalla G, Iovene B, Calvello M, Ori M, Varone F and Richeldi L 2018 Idiopathic pulmonary fibrosis: pathogenesis and management *Respiratory research* **19** 1-18
Shaker K, Häggmark I, Reichmann J, Arsenian-Henriksson M and Hertz H M 2021 Phase-contrast X-ray tomography resolves the terminal bronchioles in free-breathing mice *Communications Physics* **4** 259
Shen W, Tang K, Zhu H and Liu B 2002 New Advances in LiF: Mg, Cu, P TLD (GR-200A) *Radiation protection dosimetry* **100** 357-60
Shope T B, Gagne R M and Johnson G C 1981 A method for describing the doses delivered by transmission x-ray computed tomography *Medical physics* **8** 488-95
Slutsky A S and Ranieri V M 2013 Ventilator-induced lung injury *New England Journal of Medicine* **369** 2126-36
Smaldone G C and Mitzner W 2012 Unresolved mysteries *Journal of applied physiology* **113** 1945-7
Smith B J, Roy G S, Cleveland A, Mattson C, Okamura K, Charlebois C M, Hamlington K L, Novotny M V, Knudsen L and Ochs M 2020 Three alveolar phenotypes govern lung function in murine ventilator-induced lung injury *Frontiers in Physiology* **11** 660
Solak E 2021 A comparison between LiF, Al2O3 and NaCl pellets for luminescence dosimetry based on clinical and laboratory measurements
Spooner N, Smith B, Williams O, Creighton D, McCulloch I, Hunter P, Questiaux D and Prescott J 2011 Analysis of luminescence from common salt (NaCl) for application to retrospective dosimetry *Radiation Measurements* **46** 1856-61
Suki B and Bates J H 2011 Lung tissue mechanics as an emergent phenomenon *Journal of applied physiology* **110** 1111-8
Suortti P and Schulze C 1995 Fixed-exit monochromators for high-energy synchrotron radiation *Journal of Synchrotron Radiation* **2** 6-12
Suryadevara V, Nazeer S S, Sreedhar H, Adelaja O, Kajdacsy-Balla A, Natarajan V and Walsh M J 2020 Infrared spectral microscopy as a tool to monitor lung fibrosis development in a model system *Biomedical optics express* **11** 3996-4007
Thirion J-P 1998 Image matching as a diffusion process: an analogy with Maxwell's demons *Medical image analysis* **2** 243-60
Van Der Walt S, Colbert S C and Varoquaux G 2011 The NumPy array: a structure for efficient numerical computation *Computing in science & engineering* **13** 22-30
Van der Walt S, Schönberger J L, Nunez-Iglesias J, Boulogne F, Warner J D, Yager N, Gouillart E and Yu T 2014 scikit-image: image processing in Python *PeerJ* **2** e453
Vedam S, Keall P, Kini V, Mostafavi H, Shukla H and Mohan R 2002 Acquiring a four-dimensional computed tomography dataset using an external respiratory signal *Physics in Medicine & Biology* **48** 45
Viergever M A, Maintz J A, Klein S, Murphy K, Staring M and Pluim J P 2016 A survey of medical image registration–under review. Elsevier) pp 140-4

Vrigneaud J M, Courteau A, Ranouil J, Morgand L, Raguin O, Walker P, Oudot A, Collin B and Brunotte F 2013 Application of the optically stimulated luminescence (OSL) technique for mouse dosimetry in micro-CT imaging *Medical Physics* **40** 122102

Waldner L and Bernhardsson C 2018 Physical and dosimetric properties of NaCl pellets made in-house for the use in prospective optically stimulated luminescence dosimetry applications *Radiation measurements* **119** 52-7

Waldner L, Rääf C and Bernhardsson C 2020 NaCl pellets for prospective dosimetry using optically stimulated luminescence: Signal integrity and long-term versus short-term exposure *Radiation and environmental biophysics* **59** 693-702

Webb H H and Tierney D F 1974 Experimental pulmonary edema due to intermittent positive pressure ventilation with high inflation pressures. Protection by positive end-expiratory pressure *American Review of Respiratory Disease* **110** 556-65

White D, Buckland-Wright J, Griffith R, Rothenberg L, Showwalter C, Williams G, Wilson I and Zankl M 1992 5. Phantoms in Diagnostic Procedures *Reports of the International Commission on Radiation Units and Measurements* 26-30

Willekens I, Buls N, Lahoutte T, Baeyens L, Vanhove C, Caveliers V, Deklerck R, Bossuyt A and de Mey J 2010 Evaluation of the radiation dose in micro-CT with optimization of the scan protocol *Contrast media & molecular imaging* **5** 201-7

Zitova B and Flusser J 2003 Image registration methods: a survey *Image and vision computing* **21** 977-1000

Acknowledgements

This represents the culmination of several years of hard work and long hours. In many ways, this is just the beginning. As a kid from a small town in Oregon, I am living a life that I could only dream of when I was young, lying in the backyard and observing the stars. A quote that I am fond of is "The important thing in science is not so much to obtain new facts as to discover new ways of thinking about them." – William Lawrence Bragg. This I find true, and I believe this is exactly what we did in this work.

I would like to thank my head supervisor Dr. Lars E. Olsson for seeing something in me, as you told me once “I did not choose Sweden, Sweden chose me.” This mentality has stuck with me, and I am thankful to continue my scientific career under your leadership. There are many things yet to discover.

I would like to thank Dr. Marie Sydoff for her compassion and our scientific conversations exploring the use and functionality of *in-vivo* CT research.

I would also like to thank you to Dr. Irma Mahmutovic Persson, your expertise was critical to us “accomplishing the mission” at ESRF. I learned a significant amount about animal welfare and you helped make the work fun and not “work.”

I would also like to thank Dr. Sam Bayat for your expertise. I will never forget the long days at ESRF. The adrenaline rush and the excitement of using synchrotron light to probe deeper than humanity ever has before. Answering fundamental questions such as “How can mechanical ventilation help us breathe?” and what is occurring at the microscopic scale when it cannot.

Thank you also to the present and former colleagues at the Medical Radiation Physics department in Malmö and Lund and the BMC. My co-supervisor Dr. Martin Bech for your long career in this speciality field. I hope one day we can build a laboratory bench “mini-synchrotron” for *in-vivo* applications. I would also like to specifically thank Dr. Christian Bernhardsson, you have introduced me to the practical world of dosimetry, many dark moments in the lab fumbling around with the OSL dosemeters and cursing under my breath when I dropped one. I believe a lot of great things can and will come out of this work.

A warm thank you to Jürgen Persson at Promech Lab in Malmö for making the PMMA phantom to precise engineering requirements. This phantom paved the way to the great work of the first paper.

Thank you to Dr. Luca Fardin and Dr. Jose L. Cercos-Pita your unnoticed hard work is what brought this scientific work to fruition. I especially appreciate you responding to me on the weekends and evenings. I hope our friendship will always last.

Thank you to Dr. Alberto Bravin with your support we were able to discover new science with ESRF.

To all my friends I have made in Europe. And to my family whom I miss and love very much. Being half the world apart is not easy. Time lost is never regained. I am thankful to be given the upbringing that has given me the confidence to never stop exploring and never stop wondering what is next. This at the end was all worth it to me. Finally, I wish to thank my partner, Emelie Mattson, for enjoying this life with me and for supporting me through this PhD process.

Printed by Media-Tryck, Lund 2024 NORDIC SWAN ECOLABEL 3041 0903

Cross-modal Imaging in Lung Research

This work describes a reproducible method for evaluation of absorbed radiation doses. This method was applied to a pre-clinical *in-vivo* µCT application as a proof of concept. Additionally, within this work, for the first time, direct investigation of in-vivo alveolar micromechanics in two distinct pre-clinical lung injury models based on registration of dynamic 4DCT synchrotron phase-contrast images was performed in intact lungs. This approach will allow to investigate how micromechanical alterations influence fibrogenesis, This will provide novel insight for developing new therapies.

LUND UNIVERSITY

FACULTY OF MEDICINE

Department Medical Radiation Physics, Malmö
Faculty of Medicine
Lund University,
ISBN 978-91-8021-558-9